

A Residual Diffusion Model for High Perceptual Quality Codec Augmentation

Noor Fathima Ghouse*, Jens Petersen*, Auke Wiggers*, Tianlin Xu[†], Guillaume Sautière

{noor, jpeterse, auke, gsautie}@qti.qualcomm.com; tianlin.xu1@gmail.com

Abstract

Diffusion probabilistic models have recently achieved remarkable success in generating high quality image and video data. In this work, we build on this class of generative models and introduce a method for lossy compression of high resolution images. The resulting codec, which we call DIffusion-based Residual Augmentation Codec (DIRAC), is the first neural codec to allow smooth traversal of the rate-distortion-perception tradeoff at test time, while obtaining competitive performance with GAN-based methods in perceptual quality. Furthermore, while sampling from diffusion probabilistic models is notoriously expensive, we show that in the compression setting the number of steps can be drastically reduced.

1. Introduction

Denoising diffusion probabilistic models (DDPMs) [57] have recently shown incredible performance in the generation of high-resolution images with high perceptual quality. For example, they have powered large text-to-image models such as DALL-E 2 [49] and Imagen [55], which are capable of producing realistic high-resolution images based on arbitrary text prompts. Likewise, diffusion models have demonstrated impressive results on image-to-image tasks such as super-resolution [56, 20], deblurring [68] or inpainting [54], in many cases outperforming generative adversarial networks (GANs) [13]. Our goal in this work is to leverage these capabilities in the context of learned compression.

Neural codecs, which learn to compress from example data, are typically trained to minimize distortion between an input and a reconstruction, as well as the bitrate used to transmit the data [63]. However, optimizing for rate-distortion may result in blurry reconstructions. A recent class of generative models focuses instead on improving perceptual quality of reconstructions, either with end-to-end trained neural codecs [4, 39]—we refer to such techniques

Preprint. Qualcomm AI Research is an initiative of Qualcomm Technologies, Inc. [†]: Work completed during an internship at Qualcomm AI Research. *: Equal contribution.



Figure 1: Base reconstruction (left) and the DIRAC-enhanced version (right). Our model combines a base codec with a receiver-side enhancement model, and can smoothly interpolate between near-state-of-the-art fidelity (PSNR, higher better) and near-state-of-the-art perceptual quality (FID, lower better). For JPEG ($QF = 5$) specifically, we achieve a drastic improvement in perceptual quality without loss in PSNR. Best viewed digitally, PSNR measured on the shown example, FID/256 measured on the full CLIC 2020 test dataset.

as *generative compression*—or by using a receiver-side *perceptual enhancement* model [27] to augment the output of standard codecs. Either approach will usually come at a cost in fidelity, as there is a fundamental tradeoff between fidelity and perceptual quality [8]. Finding a good operating point for this tradeoff is not trivial and likely application-dependent. Ideally, one would like to be able to select this operating point at test time. But while adaptive rate control is commonly used, few neural image codecs allow trading off distortion and perceptual quality dynamically [25, 3].

In this work, we present a method that allows users to navigate the full rate-distortion-perception tradeoff at test time with a single model. Our approach, called *DIffusion Residual Augmentation Codec (DIRAC)*, uses a base codec to produce an initial reconstruction with minimal distortion, and then improves its perceptual quality using a de-

noising diffusion probabilistic model that predicts residuals, see Fig. 1 for an example. The intermediate samples correspond to a smooth traversal between high fidelity and high perceptual quality, so that sampling can be stopped when a desired tradeoff is reached. Recent work [72, 46] already demonstrates that a diffusion-based image codec is feasible in practice, but we show that different design choices allow us to outperform their models by a large margin, and enable faster sampling as well as selection of the distortion-perception operating point. Our contributions are:

- We demonstrate a practical and flexible diffusion-based model that can be combined with any image codec to achieve high perceptual quality compression. Paired with a neural base codec, it can interpolate between high fidelity and high perceptual quality while being competitive with the state of the art in both.
- Our model can be used as a drop-in enhancement model for traditional codecs, where we achieve strong perceptual quality improvements. For JPEG specifically, we improve FID/256 by up to 78% without loss in PSNR.
- We present techniques that make the diffusion sampling procedure more efficient: we show that in our setting we need no more than 20 sampling steps, and we introduce *rate-dependent thresholding*, which improves performance for multi-rate base codecs.

2. Related work

Neural data compression Neural network based codecs are systems that learn to compress data from examples. These codecs have seen major advances in both the image [41, 51, 5, 40] and video domain [69, 36, 52, 17, 2, 24, 23]. Most modern neural codecs are variations of *compressive autoencoders* [63], which transmit data \mathbf{x} using an autoencoder-like architecture, resulting in a reconstruction $\hat{\mathbf{x}}$. These systems are typically optimized using a rate-distortion loss, i.e. a combination of distortion and a rate loss that are balanced with a rate-parameter λ_{rate} .

Recent work identifies the importance of a third objective: *perceptual quality*, ideally meaning that reconstructions look like real data according to human observers. Blau and Michali [8] formalize perceptual quality as a distance between the image distribution $p(\mathbf{x})$ and the distribution of reconstructions $p(\hat{\mathbf{x}})$, and show that rate, distortion and perception are in a triple tradeoff. To optimize for perceptual quality, a common choice is to train the decoder as a (conditional) generative adversarial network by adding a GAN loss term to the rate-distortion loss and training a discriminator [4, 39, 75, 3, 43].

It is impractical to train and deploy one codec per rate-distortion-perception operating point. A common choice is therefore to condition the network on the bitrate trade-off parameter λ_{rate} , and vary this parameter during training [70, 60, 50]. Recent GAN-based works use similar techniques to trade off fidelity and perceptual quality, either using control parameters, or by masking the transmitted latent [70, 25, 3]. In particular, the work by Agustsson *et al.* [3] uses receiver side conditioning to trade-off distortion and realism at a particular bitrate. However, a codec that can navigate all axes of the rate-distortion-perception trade-off simultaneously using simple control parameters does not exist yet.

Diffusion probabilistic models Denoising diffusion probabilistic models (DDPMs) [57, 19] are latent variable models in which the latents $\mathbf{x}_1, \dots, \mathbf{x}_T$ are defined as a T -step Markov chain with Gaussian transitions. Through this Markov chain, the *forward process* gradually corrupts the original data \mathbf{x}_0 . The key idea of DDPMs is that, if the forward process permits efficient sampling of any variable in the chain, we can construct a generative model by learning to reverse the forward process. To generate a sample, the reverse model is applied iteratively. For a thorough description of DDPMs, we refer the reader to the appendix or Sohl-Dickstein *et al.* [57].

DDPMs have seen success in various application areas, including image and video generation [20, 21, 73, 49, 55], representation learning [48, 47], and image-to-image tasks such as super-resolution [56] and deblurring [68]. Recent work applies this model class in the context of data compression as well. Hoogeboom *et al.* [22] show that DDPMs can be used to perform lossless compression. In the lossy compression setting, Ho *et al.* [19] show that if continuous latents could be transmitted, a DDPM enables progressive coding. Theis *et al.* [62] make this approach feasible by using reverse channel coding, yet it remains impractical for high resolution images due to its high computational cost.

More practical diffusion-based approaches for lossy image compression exist, too. Yang and Mandt [72] propose a codec where a conditional DDPM takes the role of the decoder, directly producing a reconstruction from a latent variable. Pan *et al.* [46] similarly use a pretrained text-conditioned diffusion model as decoder, and let the encoder extract a text embedding. However, both approaches still require a large number of sampling steps, or encoder-side optimization of the compressed latent.

Standard codec restoration A common approach is to take a standard codec such as JPEG, and enhance or *restore* its reconstructions. Until recently, most restoration works focused on improving distortion metrics such as PSNR or SSIM [14, 32, 34, 15, 71, 74]. However, distortion-

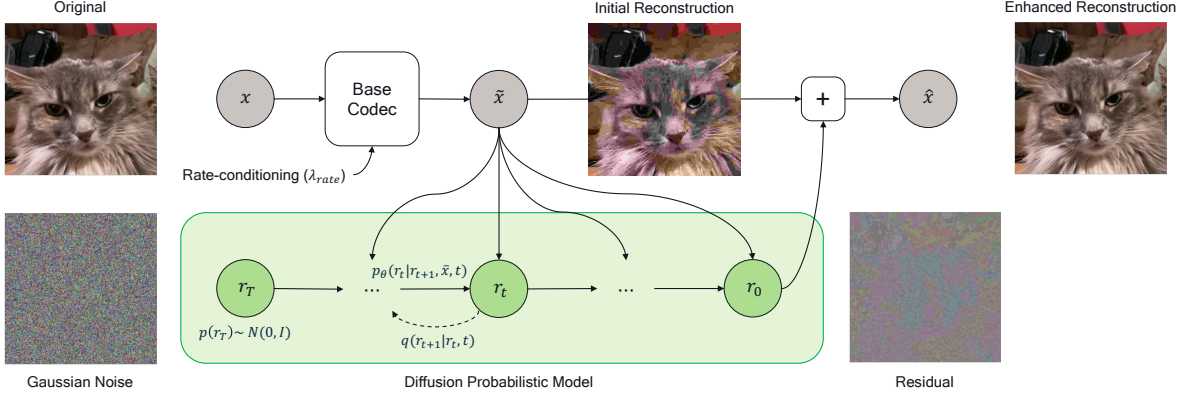


Figure 2: Overview of our architecture. Given an input image \mathbf{x} and target rate factor λ_{rate} , we obtain a base codec reconstruction $\tilde{\mathbf{x}}$. Our DDPM is conditioned on $\tilde{\mathbf{x}}$ and learns to model a reverse diffusion process that generates residuals r_0 from sampled gaussian noise latents r_T . The enhanced reconstruction $\hat{\mathbf{x}}$ is then obtained by adding the predicted residual to $\tilde{\mathbf{x}}$

optimized restoration typically leads to blurry images, as blur get rids of compression artifacts such as blocking and ringing. Consequently, a recent category of work on *perceptual enhancement* [27, 28, 54, 67, 59] focuses mainly on realism of the enhanced image. This is usually measured by perceptual distortion metrics such as LPIPS [76] or distribution-based metrics like FID [18]. Although enhanced images are less faithful to the original than the non-enhanced version, they may be rated as more realistic by human observers. In this setting, DDPMs have mostly been applied to JPEG restoration [28, 54, 59]. However, these methods have not shown test-time control of perception-distortion tradeoff, and were only tested for a single standard codec (JPEG) on low-resolution data.

3. Method

In this work, we introduce DIRAC, a diffusion-based image compression approach for high-resolution images. It combines a (potentially learned) base codec with a residual diffusion model that performs iterative enhancement. This setup is shown in Fig. 2. By design, we obtain both a high fidelity initial reconstruction, and a high perceptual quality enhanced reconstruction. The enhancement is performed on the receiver side and can be stopped at any time, enabling test-time control over the distortion-perception tradeoff.

3.1. Residual diffusion models

Diffusion-based enhancement is typically achieved by conditioning the reverse model on the image-to-enhance $\tilde{\mathbf{x}}$, effectively modeling the conditional distribution $p(\mathbf{x}_0|\tilde{\mathbf{x}})$ [20, 54, 59]. Following Whang *et al.* [68], we instead opt to model the distribution of residuals $p(\mathbf{r}_0|\tilde{\mathbf{x}})$, where $\mathbf{r}_0 = \mathbf{x} - \tilde{\mathbf{x}}$ and the index is for conceptual diffusion time. From an information theory perspective modeling residuals

is equivalent to modeling images, but residuals follow an approximately Gaussian distribution, which we believe can be easier to model. More details on this choice are given in the appendix.

For training, we use the common loss parametrization where the model learns to predict the initial sample instead of the noise that was added to it. Yang and Mandt [72] note that optimizing the perceptual distortion metric LPIPS [76] contributes to perceptual performance, and we adopt a similar practice here by adding a loss term, so that our final loss becomes:

$$\mathcal{L}(\mathbf{x}, \tilde{\mathbf{x}}) = \mathbb{E}_{t, \mathbf{r}_t} [w_t \|\mathbf{r}_0 - \mathbf{r}_0'\|^2 + \lambda_{LPIPS} d_{LPIPS}(\mathbf{x}, \tilde{\mathbf{x}} + \mathbf{r}_0')], \quad (1)$$

where $\mathbf{r}_0' = g_\theta(\mathbf{r}_t, t)$ is the prediction from our model. w_t is a weighting factor for which the theoretically derived terms become very large for small t (see appendix for the derivation), so we choose to set $w_t = 1$ to balance all loss terms evenly, similar to how Ho *et al.* [19] use a weighted variational objective in practice.

3.2. Distortion-perception traversal

The choice to enhance a base codec reconstruction with a generative model has a compelling advantage over approaches that learn to trade off rate, distortion and perception in an end-to-end manner: in theory, it gives us access to an initial reconstruction $\tilde{\mathbf{x}}$ with maximum fidelity, and an enhanced reconstruction $\hat{\mathbf{x}}$ with maximum perceptual quality. First, for a perfect encoder and decoder, $\tilde{\mathbf{x}}$ has the lowest distortion in expectation. Second, if the encoder and decoder are deterministic, and the enhancement model learns $p(\mathbf{x}|\tilde{\mathbf{x}})$ exactly, then we have $p(\hat{\mathbf{x}}) = p(\mathbf{x})$. This means perfect quality under the definition of Blau and Michali [8].

One can also view the decoder and enhancement model as one joint stochastic decoder, which is required for perfect quality at any bitrate [65]. In this picture, the diffusion steps will then gradually move the prediction from the mean of the learned distribution—which would be 0 for the residuals of an optimal base model—to a sample, corresponding to a transition from high fidelity to high perceptual quality.

3.3. Sampling improvements

In this work we make use of the noise schedule and sampling procedure introduced by Denoising Diffusion Implicit Models (DDIM) [58]. While we use $T = 1000$ diffusion steps during training, the number of sampling steps can be reduced to 100 at test time at negligible cost to performance, by redistributing the timesteps based on the scheme described by Nichol and Dhariwal [44]. As explained in the previous section, the sampling procedure can be stopped at any point, e.g. when the desired perceptual quality is achieved or when a compute budget is reached. To indicate how many sampling steps are performed, we refer to our model as DIRAC-n, going from DIRAC-1 to DIRAC-100.

We further improve sampling efficiency and performance through two contributions: late-start sampling and *rate-dependent thresholding*.

First, we demonstrate in Section 5.3 that we can skip 80% of the 100 sampling steps, instead starting sampling at DIRAC-80 with noise as model input which is scaled according to the diffusion model’s noise schedule. We are not the first to introduce late-start sampling [38], but we can do it while sampling directly from a scaled standard Gaussian as opposed to a more complex distribution, simplifying the approach. We further explain the effectiveness of this approach by showing that the sampling trajectory has very small curvature in the early steps.

Second, we make use of a method we dub *rate-dependent thresholding*. Like most diffusion works, we scale our data (which here are residuals) to the range $[-1; 1]$ and clip all intermediate predictions \mathbf{r}_0' to this range. However, the distribution of residuals strongly depends on the bit rate of the base codec, with high rate resulting in small residuals between original and reconstruction, and vice versa (see appendix for an analysis of residual distributions). Inspired by Saharia *et al.* [55], who introduce *dynamic thresholding*, we analyze the training data distribution and define a value range for each rate (more precisely, for each λ_{rate} we evaluate). Empirically we found that choosing a range such that 95% of values fall within it works best. During sampling, intermediate predictions are then clipped to the range for the given rate parameter instead of $[-1; 1]$. We hypothesize that this reduces outlier values that disproportionately affect PSNR. In Section 5.3 we show that it does indeed improve PSNR, without affecting perceptual quality. Contrary to Saharia *et al.* we only

perform clipping, but not rescaling of intermediate residuals.

We only apply rate-dependent thresholding in the generative compression setting, where we have access to λ_{rate} on the receiver-side, but not for the enhancement of traditional codecs as access to the quality factor is not guaranteed.

4. Experiments

We evaluate DIRAC both as a generative compression model by enhancing a strong neural base codec, and in the perceptual enhancement setting by using traditional codecs as base codec. In the generative compression setting, we evaluate both rate-distortion and rate-perception performance in comparison to prior work in neural compression, and demonstrate that DIRAC can smoothly traverse the entire rate-distortion-perception tradeoff. In the enhancement setting, we demonstrate DIRAC’s flexibility by comparing it with task-specific methods from the literature, focusing on both distortion and perceptual quality. Finally, we present experiments that elucidate why our proposed sampling improvements—extremely late sampling start and rate-dependent thresholding—can be successful in the residual enhancement setting.

Baselines For the generative compression setting, we focus on strong GAN-based baselines. One of the strongest perceptual codecs is *HiFiC* [39], a GAN-based codec trained for a specific rate-distortion-perception tradeoff point. *MultiRealism*, a followup work [3], allows navigating the distortion-perception tradeoff by sharing decoder weights and conditioning the decoder on the tradeoff parameter [3]. Additionally, *MS-ILM* [43] show that better discriminator design can further improve perceptual scores [43]. Finally, Yang and Mandt [72] propose a codec where a conditional DDPM takes the role of the decoder, directly producing a reconstruction from a latent variable.

In the JPEG restoration setting, we compare to *DDRM* [28], which recently outperformed the former state-of-the-art method QGAC [15]. They use a pre-trained image-to-image diffusion model and relax the diffusion process to nonlinear degradation, as introduced in [27], to enable JPEG restoration for low resolution images.

Other relevant diffusion-based baselines include *Palette* [54] and *IIGDM* [59], which explicitly train for JPEG restoration, yet only report perceptual quality on low resolution datasets. Finally, for VTM restoration, we consider *ArabicPerceptual* [67], however it is trained and evaluated on different datasets and metrics. Due to these differences, comparison to these methods can be found in the appendix.

Our models Creating a DIRAC model consists of two stages: (1) training or defining a multi-rate base codec, and (2) training a diffusion model to enhance this base codec.

In the generative compression setting, *i.e.* when the base codec is neural, we use the SwinT-CHARM [77] model. It is a near-state-of-the-art compressive autoencoder based on the Swin Transformer architecture [35]. We adapt this codec to support multiple bitrates using a technique known as *latent scaling*, see details in appendix.

In the enhancement setting, we couple DIRAC with two standard codecs as base model: the intra codec of VTM 17.0 [9], as it is one of the best performing standard codecs in the low bitrate regime, and the widely-used JPEG [66] codec. Later, we refer to SwinT-CHARM+DIRAC as just DIRAC, while we explicitly refer to VTM+DIRAC and JPEG+DIRAC.

Metrics and evaluation We evaluate our method using both distortion metrics and perceptual quality metrics. We always evaluate on full resolution RGB images: we replicate-pad the network input so that all sides are multiple of the total downsampling factor of the network, and crop the output back to the original resolution. We repeat scores as reported in the respective publications.

To measure distortion, we use the common PSNR metric. We also include the full-reference LPIPS [76] metric as it has been shown to align well with human judgment of visual quality. As perceptual quality metrics, we primarily use a variation of the Frechet Inception Distance (FID) [18] metric, which measures the distance between the target distribution $p(\mathbf{x})$ and the distribution of reconstructions $p(\hat{\mathbf{x}})$. FID requires resizing of input images to a fixed resolution, which for high-resolution images will destroy generated details. We therefore follow procedure of previous compression work and use half-overlapping 256×256 crops [39, 3, 43] for high resolution datasets, this metric is referred to as FID/256.

When we report bitrates, we perform entropy coding and take the file size. This leads to no more than 0.5% overhead compared to the theoretical bitrate given by the prior.

Datasets To train the SwinT-CHARM base model and residual diffusion models, we use the training split of the high-resolution CLIC2020 dataset [64] (1633 images of varying resolutions). For DDPM training, we follow the three-step preprocessing pipeline of HiFiC [39]: for each image, randomly resize according to a scale factor uniformly sampled from the range $[0.5, 1.0]$, then take a random 256×256 crop, then perform a horizontal flip with probability 0.5. For validation and model selection, we use the CLIC 2020 validation set (102 images).

We evaluate on two common image compression benchmark datasets: the CLIC2020 test set (428 images) and

the Kodak dataset [31] (24 images). To enable comparison with enhancement literature, we evaluate on the low resolution ImageNet-val1k [12, 45]. We follow the preprocessing procedure from Kawar *et al.* [28] where images are center cropped along the long edge and then resized to 256.

Implementation details For the base codec, we implement SwinT-CHARM as described in the original paper. We first train a single rate model for 2M iterations on 256×256 CLIC 2020 train crops, then finetune it for multiple bitrates for 0.5M iterations. The standard base codecs are evaluated using the VTM reference software, CompressAI framework [6] and libjpeg in Pillow. We provide full details on the implementation and hyperparameters in the appendix.

The diffusion residual model is based off DDPM’s official open source implementation [13], and we base most of our default architecture settings on the 256×256 DDPM from Preechakul *et al.* [48], which uses a U-Net architecture [53]. Conditioning on the base codec reconstruction $\hat{\mathbf{x}}$ is achieved by concatenating $\hat{\mathbf{x}}$ and the DDPM latent \mathbf{r}_t in each step. Our model has 108.4 million parameters. For context, the HiFiC baseline has 181.5 million. As HiFiC requires only one forward pass to create a reconstruction, it is typically less expensive than DIRAC. We provide more detail on computational cost in the appendix.

Finally DIRAC and VTM+DIRAC diffusion models are trained for 650k steps, using the Adam optimizer [29] with a learning rate of 10^{-4} and no learning rate decay. The JPEG+DIRAC model was trained for 1M iterations, as JPEG degradations are much more severe than those of VTM and SwinT-CHARM.

5. Results

5.1. Generative compression

We visualize the rate-distortion and rate-perception tradeoffs in Fig. 3. We show our model in two configurations: DIRAC-100 (100 sampling steps) has maximum perceptual quality, and DIRAC-1 (single sampling step) has minimal distortion.

Along the distortion axis, *i.e.* PSNR, DIRAC-1 is close to VTM and *MultiRealism*[3] at $\beta = 0$, which in turn is competitive with the state of the art. On the perceptual quality side, HiFiC is the current state of the art of peer-reviewed works. DIRAC-100 matches HiFiC in FID/256 with better PSNR on both test datasets. Likewise, we match *MultiRealism* at $\beta = 2.56$ in FID/256. Note that between DIRAC and *MultiRealism*, no model is strictly better than the other, *i.e.* better on both distortion and perception axes at the same time. This is reflected in the examples in Fig. 4, where DIRAC-1, our high-fidelity model, looks a bit sharper than [3], while examples with high perceptual quality are hardly distinguishable.

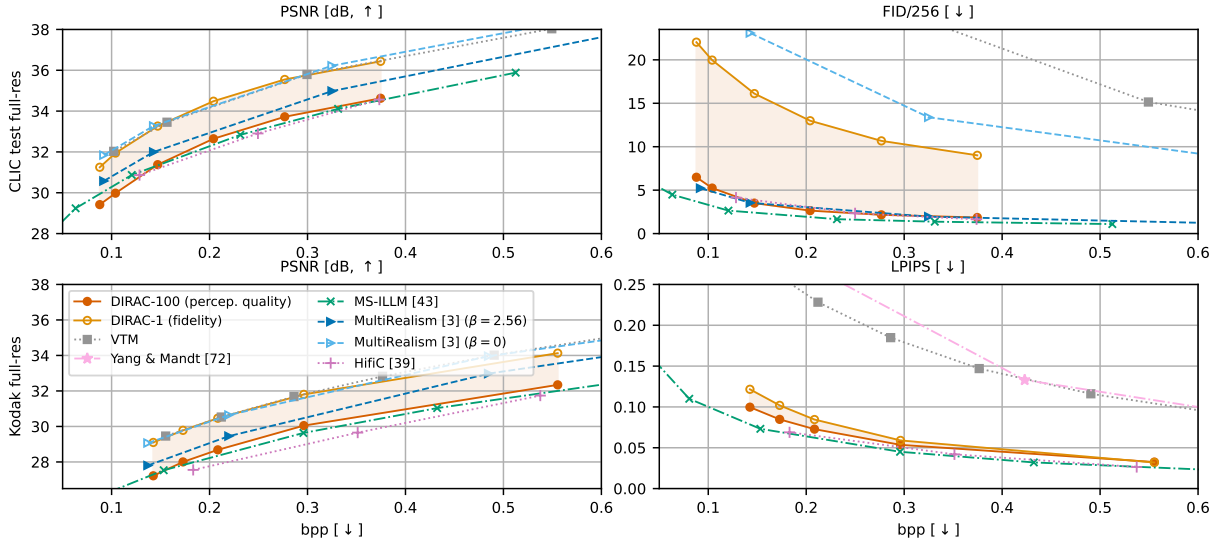


Figure 3: Rate-distortion (left) and rate-perception (right) curves for the CLIC2020 test set (top) and Kodak dataset (bottom). The Kodak dataset has too few samples for FID/256 evaluation, instead we evaluate LPIPS, a perceptual distortion metric.

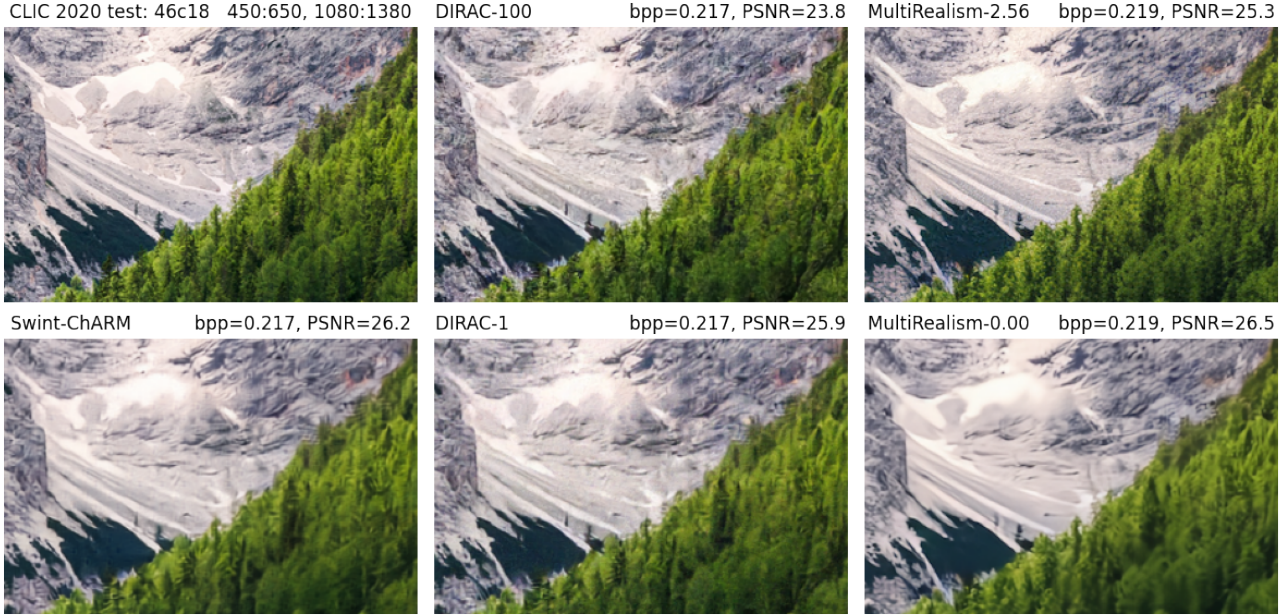


Figure 4: CLIC 2020 test reconstructions comparing our model to *MultiRealism*[3]. We show original (top left), Swint-ChARM base codec (bottom left), DIRAC-1 (high fidelity) and DIRAC-100 (high perceptual quality) in center column, *MultiRealism* counterparts in right column. Shown scores are for full image. Best viewed electronically.

MS-ILLM [43] achieves a new state of the art in FID/256 and is unmatched by all other methods, but upon qualitative comparison in Fig. 5 we observe that even at a lower bitrate compared to MS-ILLM, DIRAC-100 is able to generate perceptually relevant details in a more meaningful manner. Of course, this is only a single datapoint, and stronger claims require a thorough perceptual comparison. Similar to Multi-

realism [3], our model can target a wide range of distortion-perception tradeoffs at test time, indicated by the shaded area in Fig. 3. Finally, we compare to the diffusion-based codec of Yang and Mandt [72] on Kodak. Our model outperforms theirs by a large margin in terms of LPIPS. More visual examples can be found in the appendix.



Figure 5: CLIC 2020 test reconstruction by DIRAC-100 and MS-ILLM, crop location chosen based on [43].

5.2. Enhancement of standard codecs

We evaluate enhancement of two standard codecs: JPEG and VTM. In Fig. 6 we compare JPEG+DIRAC to literature on the low-resolution dataset ImageNet-1K (left panels) and evaluate JPEG+DIRAC and VTM+DIRAC on the high-resolution dataset CLIC test 2020 (right panels).

When comparing to enhancement literature (left panels in Fig. 6), we compare to QGAC and DDRM, specifically their scores resulting from averaging 8 independent samples, denoted DDRM (A). JPEG+DIRAC-1 slightly outperforms the competing methods in the low rate regime in terms of PSNR, while improving LPIPS by a large margin. Further sampling allows JPEG+DIRAC-100 to improve LPIPS, at the cost of PSNR. While the difference in LPIPS seem small, qualitatively the textures in JPEG+DIRAC-100 are much better than in JPEG+DIRAC-1, as can be seen in the appendix.

When evaluating JPEG+DIRAC and VTM+DIRAC on the high-resolution dataset CLIC test 2020 (right panels in Fig. 6), we can see that both VTM+DIRAC-1 and JPEG+DIRAC-1 outperform their base codec in fidelity. In the perceptual enhancement setting, both VTM+DIRAC-100 and JPEG+DIRAC-100 far outperform their base codec in FID/256, specifically at the lowest rate, with a 81% and 78% improvement respectively. DIRAC offers a consistent boost in perceptual quality, even as one improves the base codec from JPEG to VTM. We show visual examples of both systems in the middle panels, showing a drastic improvement in visual quality. Notice the lack of texture on the top samples, which are from distortion-optimized codecs. For VTM, the bottom sample has higher distortion (i.e. lower PSNR), yet looks far better to the human observer.

5.3. Sampling analysis

Reverse sampling in diffusion models is equivalent to integrating a stochastic differential equation [61]. The error incurred in the numerical approximation of the true solution trajectory will generally be proportional to its curvature

[26], meaning parts with low curvature can be integrated with few and large update steps.

In Fig. 7 (left panel) we show the average curvature of sampling trajectories for our model on the CLIC 2020 val dataset, using 100 DDIM steps [58]. Because computing the Hessian is not feasible for the number of dimensions our model operates in, we approximate it with the angle between consecutive update vectors $c = \cos^{-1}(\mathbf{u}_t \mathbf{u}_{t-1} / \|\mathbf{u}_t\| \cdot \|\mathbf{u}_{t-1}\|)$, where $u_t \propto (\mathbf{r}_0'(t) - \mathbf{r}_t)$ points from the current diffusion latent to the current prediction of the residual. We find that the curvature is small along a vast majority of steps in the sampling trajectory, meaning it is indeed possible to take a single large update step and only incur a small error.

Moreover, we find that instead of starting from standard normal noise at time T and taking a large integration step to time $t \ll T$, it is sufficient to start directly at t , using noise as input to the model that is scaled according to the diffusion model's noise schedule. In our experiments, starting sampling at $t = 20$ was a good tradeoff, with final performance almost identical to the full 100 steps (as seen in the center and right panels of Fig. 7), but saving 80% of required compute. One might suspect that the above is due to a suboptimal noise schedule (we use the popular *linear* schedule), but we explored several different schedules as well as noise schedule learning [30] and found no improvement in performance.

Besides showing that our model can work efficiently using at most 20 sampling steps, in the generative compression setting we also introduce a concept we call *rate-dependent thresholding*, which we detail in Section 3.3. By clipping each intermediate residual prediction to a percentile-range obtained from the training data (we define the range to include 95% of the data at a given rate), we find that we can improve PSNR while not affecting FID. This can be seen in the center and right panels of Fig. 7, which also shows how our model performs a smooth traversal between high fidelity (high PSNR) and high perceptual quality (low FID/256).

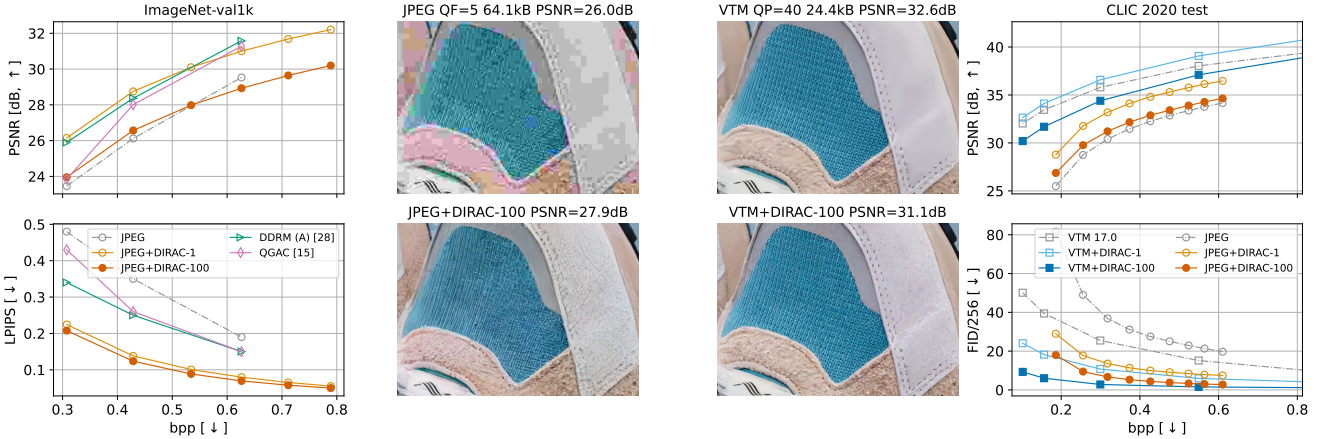


Figure 6: Quantitative results for JPEG+ and VTM+DIRAC on ImageNet-val1k (left) and CLIC test 2020 (right) respectively. We show rate-distortion (top) and rate-perception (bottom) curves. Qualitative sample is image “3f273e” in CLIC 2020 test.

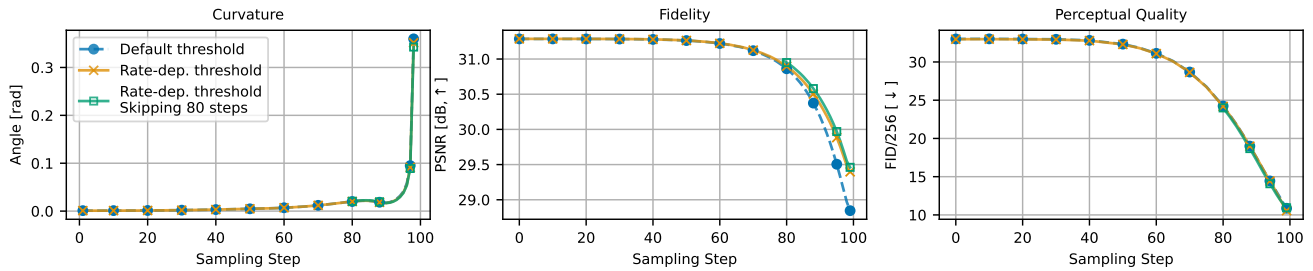


Figure 7: Analysis of the curvature of the sampling trajectory (approximated by the angle between update vectors), as well as the change in PSNR and FID/256 during sampling. All evaluations done on the CLIC 2020 val subset.

6. Discussion and Limitations

In this work, we propose a new neural image compression method called Diffusion-based Residual Augmentation Codec (DIRAC). Our approach uses a variable bitrate base codec to transmit an initial reconstruction with high fidelity to the original input, and then uses a diffusion probabilistic model to improve its perceptual quality. We show that this design choice enables fine control over the rate-distortion-perception tradeoff at test time, which for example enables users to choose if an image should be decoded with high fidelity or high perceptual quality. Paired with a strong neural codec as base model, we can smoothly interpolate between performance that is competitive with the state of the art in either fidelity or perceptual quality. Our model can also work as a receiver-side enhancement model for traditional codecs, drastically improving perceptual quality at sometimes no cost in PSNR. Finally, we demonstrate that our model can work with 20 sampling steps or less, and propose *rate-dependent thresholding*, which improves PSNR of the diffusion model without affecting perceptual quality in the multi-rate setting.

Limitations Although our model gives the user control over the amount of hallucinated content, we currently do not control *where* such hallucinations occur. Similar to GAN-based codecs, we observe that increasing perception sometimes harms fidelity in small regions with semantically important content, such as faces and text. Addressing this limitation is an important next step for generative codecs. Additionally, it is fairly expensive to use a DDPM on the receiver side. Although we drastically reduce the number of sampling steps, HiFiC and its variations [39, 3] are less expensive to run. We provide more details on computational cost in the appendix. On the other hand, sampling efficiency of diffusion models is a major research direction, and we expect our approach to benefit from these advances.

Acknowledgments

We thank Johann Brehmer, Taco Cohen, Yunfan Zhang, Hoang Le for useful discussions and reviews of early drafts of the paper. Thanks to Fabian Mentzer for instructions on reproducing HiFiC, and to Matthew Muckley for providing the MS-ILLM reconstructions and scores.

References

[1] Enhance Compression Model (ECM). <https://vcgit.hhi.fraunhofer.de/ecm/ECM>, Accessed March 10, 2023. 16

[2] Eirikur Agustsson, David Minnen, Nick Johnston, Johannes Balle, Sung Jin Hwang, and George Toderici. Scale-space flow for end-to-end optimized video compression. In *Proceedings of the IEEE conference on Computer Vision and Pattern Recognition*, 2020. 2

[3] Eirikur Agustsson, David Minnen, George Toderici, and Fabian Mentzer. Multi-realism image compression with a conditional generator. *arXiv preprint arXiv:2212.13824*, 2022. 1, 2, 4, 5, 6, 8, 19, 22

[4] Eirikur Agustsson, Michael Tschannen, Fabian Mentzer, Radu Timofte, and Luc Van Gool. Generative adversarial networks for extreme learned image compression. In *Proceedings of the IEEE conference on Computer Vision and Pattern Recognition*, 2019. 1, 2

[5] Johannes Ballé, David Minnen, Saurabh Singh, Sung Jin Hwang, and Nick Johnston. Variational image compression with a scale hyperprior. In *International Conference on Learning Representations*, 2018. 2, 14, 15

[6] Jean Bégaït, Fabien Racapé, Simon Feltman, and Akshay Pushparaja. CompressAI: a PyTorch library and evaluation platform for end-to-end compression research. *arXiv preprint arXiv:2011.03029*, 2020. 5, 14, 15

[7] Mikołaj Bińkowski, Danica J. Sutherland, Michael Arbel, and Arthur Gretton. Demystifying mmd gans. In *International Conference on Learning Representations*, Feb 2022. 16

[8] Yochai Blau and Tomer Michaeli. Rethinking lossy compression: The rate-distortion-perception tradeoff. In *International Conference on Machine Learning*, pages 675–685. PMLR, 2019. 1, 2, 3, 13

[9] Benjamin Bross, Ye-Kui Wang, Yan Ye, Shan Liu, Jianle Chen, Gary J Sullivan, and Jens-Rainer Ohm. Overview of the versatile video coding (VVC) standard and its applications. *IEEE Transactions on Circuits and Systems for Video Technology*, 31(10):3736–3764, 2021. 5

[10] Tong Chen and Zhan Ma. Variable bitrate image compression with quality scaling factors. In *ICASSP 2020-2020 IEEE International Conference on Acoustics, Speech and Signal Processing (ICASSP)*, pages 2163–2167. IEEE, 2020. 15

[11] Kamil Deja, Anna Kuzina, Tomasz Trzcinski, and Jakub M Tomezak. On analyzing generative and denoising capabilities of diffusion-based deep generative models. *Neural Information Processing Systems*, 2022. 13

[12] Jia Deng, Wei Dong, Richard Socher, Li-Jia Li, Kai Li, and Li Fei-Fei. Imagenet: A large-scale hierarchical image database. In *2009 IEEE Conference on Computer Vision and Pattern Recognition*, pages 248–255, 2009. 5

[13] Prafulla Dhariwal and Alexander Nichol. Diffusion models beat GANs on image synthesis. In *Advances in Neural Information Processing Systems*, volume 34, pages 8780–8794, 2021. 1, 5, 14, 16

[14] Chao Dong, Yubin Deng, Chen Change Loy, and Xiaoou Tang. Compression artifacts reduction by a deep convolutional network. In *2015 IEEE International Conference on Computer Vision (ICCV)*, Dec 2015. 2

[15] Max Ehrlich, Larry Davis, Ser-Nam Lim, and Abhinav Shrivastava. Quantization guided jpeg artifact correction. In *European Conference on Computer Vision*, pages 293–309, 2020. 2, 4, 13

[16] Zongyu Guo, Zhizheng Zhang, Runsen Feng, and Zhibo Chen. Soft then hard: Rethinking the quantization in neural image compression. In *International Conference on Machine Learning*, pages 3920–3929. PMLR, 2021. 15

[17] Amirhossein Habibian, Ties van Rozendaal, Jakub M Tomczak, and Taco S Cohen. Video compression with rate-distortion autoencoders. In *IEEE International Conference on Computer Vision*, 2019. 2

[18] Martin Heusel, Hubert Ramsauer, Thomas Unterthiner, Bernhard Nessler, and Sepp Hochreiter. GANs Trained by a Two Time-Scale Update Rule Converge to a Local Nash Equilibrium, 2017. 3, 5

[19] Jonathan Ho, Ajay Jain, and Pieter Abbeel. Denoising diffusion probabilistic models. *Advances in Neural Information Processing Systems*, 33:6840–6851, 2020. 2, 3, 12, 13

[20] Jonathan Ho, Chitwan Saharia, William Chan, David J Fleet, Mohammad Norouzi, and Tim Salimans. Cascaded diffusion models for high fidelity image generation. *Journal of Machine Learning Research*, 23:47–1, 2022. 1, 2, 3

[21] Jonathan Ho, Tim Salimans, Alexey A Gritsenko, William Chan, Mohammad Norouzi, and David J Fleet. Video diffusion models. In *ICLR Workshop on Deep Generative Models for Highly Structured Data*, 2022. 2

[22] Emiel Hoogeboom, Alexey A Gritsenko, Jasmijn Bastings, Ben Poole, Rianne van den Berg, and Tim Salimans. Autoregressive diffusion models. In *International Conference on Learning Representations*, 2021. 2

[23] Zhihao Hu, Guo Lu, Jinyang Guo, Shan Liu, Wei Jiang, and Dong Xu. Coarse-to-fine deep video coding with hyperprior-guided mode prediction. In *Proceedings of the IEEE conference on Computer Vision and Pattern Recognition*, 2022. 2

[24] Zhihao Hu, Guo Lu, and Dong Xu. FVC: A new framework towards deep video compression in feature space. In *Proceedings of the IEEE/CVF Conference on Computer Vision and Pattern Recognition*, pages 1502–1511, 2021. 2

[25] Shoma Iwai, Tomo Miyazaki, Yoshihiro Sugaya, and Shinichiro Omachi. Fidelity-controllable extreme image compression with generative adversarial networks. In *2020 25th International Conference on Pattern Recognition (ICPR)*, pages 8235–8242. IEEE, 2021. 1, 2

[26] Tero Karras, Miika Aittala, Timo Aila, and Samuli Laine. Elucidating the design space of diffusion-based generative models. In *Neural Information Processing Systems*, 2022. 7

[27] Bahjat Kawar, Michael Elad, Stefano Ermon, and Jiaming Song. Denoising diffusion restoration models. In *ICLR Workshop on Deep Generative Models for Highly Structured Data*, 2022. 1, 3, 4, 16

[28] Bahjat Kawar, Jiaming Song, Stefano Ermon, and Michael Elad. JPEG artifact correction using denoising diffusion

restoration models. *arXiv preprint arXiv:2209.11888*, 2022. 3, 4, 5, 13, 14, 16

[29] Diederik P Kingma and Jimmy Ba. Adam: A method for stochastic optimization. In *International Conference on Learning Representations*, 2015. 5

[30] Diederik P Kingma, Tim Salimans, Ben Poole, and Jonathan Ho. Variational diffusion models. In *Advances in Neural Information Processing Systems*, 2021. 7

[31] Photocd dataset Kodak. Kodak photocd dataset, 1991. 5

[32] Nojun Kwak, Jaeyoung Yoo, and Sang-ho Lee. Image restoration by estimating frequency distribution of local patches. *2018 IEEE/CVF Conference on Computer Vision and Pattern Recognition*, Jun 2018. 2

[33] Gustav Larsson, Michael Maire, and Gregory Shakhnarovich. Learning representations for automatic colorization. In *Computer Vision–ECCV 2016: 14th European Conference, Amsterdam, The Netherlands, October 11–14, 2016, Proceedings, Part IV* 14, pages 577–593. Springer, 2016. 14

[34] Jiaying Liu, Dong Liu, Wenhan Yang, Sifeng Xia, Xiaoshuai Zhang, and Yuanying Dai. A comprehensive benchmark for single image compression artifact reduction. *IEEE Transactions on Image Processing*, 29:7845–7860, 2020. 2

[35] Ze Liu, Yutong Lin, Yue Cao, Han Hu, Yixuan Wei, Zheng Zhang, Stephen Lin, and Baining Guo. Swin transformer: Hierarchical vision transformer using shifted windows. In *Proceedings of the IEEE/CVF international conference on computer vision*, pages 10012–10022, 2021. 5, 15

[36] Guo Lu, Wanli Ouyang, Dong Xu, Xiaoyun Zhang, Chunlei Cai, and Zhiyong Gao. DVC: An end-to-end deep video compression framework. In *Proceedings of the IEEE conference on Computer Vision and Pattern Recognition*, 2019. 2

[37] Yadong Lu, Yinhao Zhu, Yang Yang, Amir Said, and Taco S Cohen. Progressive neural image compression with nested quantization and latent ordering. *arXiv preprint arXiv:2102.02913*, 2021. 15

[38] Zhaoyang Lyu, Xudong Xu, Ceyuan Yang, Dahua Lin, and Bo Dai. Accelerating diffusion models via early stop of the diffusion process. *arXiv preprint arXiv:2205.12524*, 2022. 4, 13

[39] Fabian Mentzer, George Toderici, Michael Tschannen, and Eirikur Agustsson. High-fidelity generative image compression. In *Neural Information Processing Systems*, 2020. 1, 2, 4, 5, 8, 19

[40] David Minnen, Johannes Ballé, and George Toderici. Joint autoregressive and hierarchical priors for learned image compression. *Neural Information Processing Systems*, 2018. 2

[41] David Minnen, George Toderici, Michele Covell, Troy Chinen, Nick Johnston, Joel Shor, Sung Jin Hwang, Damien Vincent, and Saurabh Singh. Spatially adaptive image compression using a tiled deep network. In *2017 IEEE International Conference on Image Processing (ICIP)*, pages 2796–2800. IEEE, 2017. 2

[42] Anish Mittal, Rajiv Soundararajan, and Alan C. Bovik. Making a “completely blind” image quality analyzer. *IEEE Signal Processing Letters*, 20(3):209–212, Mar 2013. 16

[43] Matthew J Muckley, Alaaeldin El-Nouby, Karen Ullrich, Hervé Jégou, and Jakob Verbeek. Improving statistical fidelity for neural image compression with implicit local likelihood models. *arXiv preprint arXiv:2301.11189*, 2023. 2, 4, 5, 6, 7, 16, 19, 22

[44] Alexander Quinn Nichol and Prafulla Dhariwal. Improved denoising diffusion probabilistic models. In *International Conference on Machine Learning*, pages 8162–8171. PMLR, 2021. 4, 12, 13, 16, 17

[45] Xingang Pan, Xiaohang Zhan, Bo Dai, Dahua Lin, Chen Change Loy, and Ping Luo. Exploiting deep generative prior for versatile image restoration and manipulation. *IEEE Transactions on Pattern Analysis and Machine Intelligence*, 44(11):7474–7489, 2021. 5, 13

[46] Zhihong Pan, Xin Zhou, and Hao Tian. Extreme generative image compression by learning text embedding from diffusion models. *arXiv preprint arXiv:2211.07793*, 2022. 2

[47] Kushagra Pandey, Avideep Mukherjee, Piyush Rai, and Abhishek Kumar. DiffuseVAE: Efficient, controllable and high-fidelity generation from low-dimensional latents. *arXiv preprint arXiv:2201.00308*, 2022. 2

[48] Konpat Preechakul, Nattanat Chatthee, Suttisak Wizadwongsu, and Supasorn Suwajanakorn. Diffusion autoencoders: Toward a meaningful and decodable representation. In *Proceedings of the IEEE/CVF Conference on Computer Vision and Pattern Recognition*, pages 10619–10629, 2022. 2, 5, 16

[49] Aditya Ramesh, Prafulla Dhariwal, Alex Nichol, Casey Chu, and Mark Chen. Hierarchical text-conditional image generation with clip latents, 2022. 1, 2

[50] Oren Rippel, Alexander G Anderson, Kedar Tatwawadi, Sanjay Nair, Craig Lytle, and Lubomir Bourdev. ELF-VC: Efficient Learned Flexible-Rate Video Coding. *Neural Information Processing Systems*, 2021. 2, 15

[51] Oren Rippel and Lubomir Bourdev. Real-Time adaptive image compression. In Doina Precup and Yee Whye Teh, editors, *Proceedings of the 34th International Conference on Machine Learning*, volume 70 of *Proceedings of Machine Learning Research*, pages 2922–2930. PMLR, 2017. 2

[52] Oren Rippel, Sanjay Nair, Carissa Lew, Steve Branson, Alexander G. Anderson, and Lubomir Bourdev. Learned video compression. In *IEEE International Conference on Computer Vision*, October 2019. 2

[53] O. Ronneberger, P. Fischer, and T. Brox. U-net: Convolutional networks for biomedical image segmentation. In *Medical Image Computing and Computer-Assisted Intervention (MICCAI)*, volume 9351 of *LNCS*, pages 234–241. Springer, 2015. (available on arXiv:1505.04597 [cs.CV]). 5

[54] Chitwan Saharia, William Chan, Huiwen Chang, Chris Lee, Jonathan Ho, Tim Salimans, David Fleet, and Mohammad Norouzi. Palette: Image-to-image diffusion models. In *ACM SIGGRAPH 2022 Conference Proceedings*, pages 1–10, 2022. 1, 3, 4, 14, 16

[55] Chitwan Saharia, William Chan, Saurabh Saxena, Lala Li, Jay Whang, Emily Denton, Seyed Kamvar Seyed Ghasemipour, Bureu Karagol Ayan, S. Sara Mahdavi, Rapha Gontijo Lopes, Tim Salimans, Jonathan Ho, David J

Fleet, and Mohammad Norouzi. Photorealistic text-to-image diffusion models with deep language understanding, 2022. 1, 2, 4

[56] Chitwan Saharia, Jonathan Ho, William Chan, Tim Salimans, David J Fleet, and Mohammad Norouzi. Image super-resolution via iterative refinement. *IEEE Transactions on Pattern Analysis and Machine Intelligence*, 2022. 1, 2

[57] Jascha Sohl-Dickstein, Eric Weiss, Niru Maheswaranathan, and Surya Ganguli. Deep unsupervised learning using non-equilibrium thermodynamics. In *International Conference on Machine Learning*, pages 2256–2265. PMLR, 2015. 1, 2, 12

[58] Jiaming Song, Chenlin Meng, and Stefano Ermon. Denoising diffusion implicit models. In *International Conference on Learning Representations*, 2020. 4, 7

[59] Jiaming Song, Arash Vahdat, Morteza Mardani, and Jan Kautz. Pseudoinverse-guided diffusion models for inverse problems. In *International Conference on Learning Representations*, 2023. 3, 4, 14, 16

[60] Myungseo Song, Jinyoung Choi, and Bohyung Han. Variable-rate deep image compression through spatially-adaptive feature transform. In *Proceedings of the IEEE/CVF International Conference on Computer Vision*, pages 2380–2389, 2021. 2, 15

[61] Yang Song, Jascha Sohl-Dickstein, Diederik P. Kingma, Abhishek Kumar, Stefano Ermon, and Ben Poole. Score-based generative modeling through stochastic differential equations. In *International Conference on Learning Representations*, 2020. 7

[62] Lucas Theis, Tim Salimans, Matthew D Hoffman, and Fabian Mentzer. Lossy Compression with Gaussian Diffusion. *arXiv preprint arXiv:2206.08889*, 2022. 2

[63] Lucas Theis, Wenzhe Shi, Andrew Cunningham, and Ferenc Huszár. Lossy image compression with compressive autoencoders. *International Conference on Learning Representations*, 2017. 1, 2

[64] George Toderici, Wenzhe Shi, Radu Timofte, Lucas Theis, Johannes Balle, Eirikur Agustsson, Nick Johnston, and Fabian Mentzer. Workshop and challenge on learned image compression (clic2020). In *Proceedings of the IEEE conference on Computer Vision and Pattern Recognition*. CVPR, 2020. 5, 14

[65] Michael Tschannen, Eirikur Agustsson, and Mario Lucic. Deep generative models for distribution-preserving lossy compression. *Advances in neural information processing systems*, 31, 2018. 4

[66] Gregory K. Wallace. The JPEG Still Picture Compression Standard. *Commun. ACM*, 1991. 5

[67] Huairui Wang, Guangjie Ren, Tong Ouyang, Junxi Zhang, Wenwei Han, Zizheng Liu, and Zhenzhong Chen. Perceptual in-loop filter for image and video compression. In *2022 IEEE/CVF Conference on Computer Vision and Pattern Recognition Workshops (CVPRW)*, page 1769–1772, Jun 2022. 3, 4, 14, 16

[68] Jay Whang, Mauricio Delbracio, Hossein Talebi, Chitwan Saharia, Alexandros G Dimakis, and Peyman Milanfar. Deblurring via stochastic refinement. In *Proceedings of the IEEE/CVF Conference on Computer Vision and Pattern Recognition*, pages 16293–16303, 2022. 1, 2, 3

[69] Chao-Yuan Wu, Nayan Singhal, and Philipp Krähenbühl. Video compression through image interpolation. *Proceedings of the European Conference on Computer Vision*, 2018. 2

[70] Lirong Wu, Kejie Huang, and Haibin Shen. A GAN-based tunable image compression system. In *Proceedings of the IEEE/CVF Winter Conference on Applications of Computer Vision*, pages 2334–2342, 2020. 2

[71] Ren Yang. Ntire 2021 challenge on quality enhancement of compressed video: Methods and results. In *Proceedings of the IEEE/CVF Conference on Computer Vision and Pattern Recognition*, pages 647–666, 2021. 2

[72] Ruihan Yang and Stephan Mandt. Lossy image compression with conditional diffusion models. *arXiv preprint arXiv:2209.06950*, 2022. 2, 3, 4, 6

[73] Ruihan Yang, Prakhar Srivastava, and Stephan Mandt. Diffusion probabilistic modeling for video generation. *arXiv preprint arXiv:2203.09481*, Mar 2022. 2

[74] Ren Yang, Radu Timofte, Meisong Zheng, Qunliang Xing, Minglang Qiao, Mai Xu, Lai Jiang, Huaida Liu, Ying Chen, Youcheng Ben, et al. Ntire 2022 challenge on super-resolution and quality enhancement of compressed video: Dataset, methods and results. In *Proceedings of the IEEE/CVF Conference on Computer Vision and Pattern Recognition*, pages 1221–1238, 2022. 2

[75] Ren Yang, Luc Van Gool, and Radu Timofte. Perceptual learned video compression with recurrent conditional GAN. *arXiv preprint arXiv:2109.03082*, Sept. 2021. 2

[76] Richard Zhang, Phillip Isola, Alexei A. Efros, Eli Shechtman, and Oliver Wang. The Unreasonable Effectiveness of Deep Features as a Perceptual Metric. *2018 IEEE/CVF Conference on Computer Vision and Pattern Recognition*, 2018. 3, 5

[77] Yinhao Zhu, Yang Yang, and Taco Cohen. Transformer-based transform coding. In *International Conference on Learning Representations*, Mar 2022. 5, 14, 15

A. Method

A.1. Derivation of DDPM loss

For completeness, we show the derivation of the objective when a diffusion model learns to predict \mathbf{x}_0 directly (equivalently, \mathbf{r}_0). This is not a new contribution, and a similar derivation can be found for example in the work of Nichol and Dhariwal [44].

Following Sohl-Dickstein *et al.* [57], the ELBO on the log likelihood of $p_\theta(\mathbf{x}_0)$ can be written as T -step Kullback–Leibler (KL) divergences: $KL(q(\mathbf{x}_{t-1}|\mathbf{x}_t, \mathbf{x}_0) || p_\theta(\mathbf{x}_{t-1}|\mathbf{x}_t))$ for $t = 1, \dots, T-1$. Under the assumption that the two distributions of interest are both Gaussian, we further assume $\Sigma_\theta(\mathbf{x}_t, t) = \sigma_t^2 \mathbf{I}$ to be time dependent constants. This reduces the KL divergence at step t to a comparison from the model mean to the posterior mean of the forward process:

$$KL(q(\mathbf{x}_{t-1}|\mathbf{x}_t, \mathbf{x}_0) || p_\theta(\mathbf{x}_{t-1}|\mathbf{x}_t)) = \quad (2)$$

$$\mathbb{E}_q \left[\frac{1}{2\sigma_t^2} \|\tilde{\mu}_t(\mathbf{x}_t, \mathbf{x}_0) - \mu_\theta(\mathbf{x}_t, t)\|^2 \right] + C, \quad (3)$$

where C is a constant, and $\tilde{\mu}_t$ denotes the posterior mean of the forward process conditioned on the data input \mathbf{x}_0 , i.e., $q(\mathbf{x}_{t-1}|\mathbf{x}_t, \mathbf{x}_0)$.

Note that, using the Bayes’ rule and the Markovian property of the forward process, we can rewrite

$$\begin{aligned} q(\mathbf{x}_{t-1}|\mathbf{x}_t, \mathbf{x}_0) &= \frac{q(\mathbf{x}_{t-1}, \mathbf{x}_t|\mathbf{x}_0)}{q(\mathbf{x}_t|\mathbf{x}_0)} \\ &= \frac{q(\mathbf{x}_{t-1}|\mathbf{x}_0)q(\mathbf{x}_t|\mathbf{x}_{t-1})}{q(\mathbf{x}_t|\mathbf{x}_0)}, \end{aligned} \quad (4)$$

where the distribution $q(\mathbf{x}_t|\mathbf{x}_0) = \mathcal{N}(\mathbf{x}_t; \sqrt{\bar{\alpha}_t} \mathbf{x}_0, (1 - \bar{\alpha}_t) \mathbf{I})$ with $\alpha_t := 1 - \beta_t$ and $\bar{\alpha}_t := \prod_{s=1}^t \alpha_s$. The α_t/β_t are typically chosen empirically and referred to as the *noise schedule*.

With the known distribution of $q(\mathbf{x}_t|\mathbf{x}_0)$, we can sample \mathbf{x}_t at an arbitrary step t :

$$\mathbf{x}_t(\mathbf{x}_0, \epsilon) = \sqrt{\bar{\alpha}_t} \mathbf{x}_0 + \sqrt{1 - \bar{\alpha}_t} \epsilon, \quad \epsilon \sim \mathcal{N}(\mathbf{0}, \mathbf{I}). \quad (5)$$

Now each of the components on the RHS of Eq. (4) is defined as a Gaussian distribution with known parameters. As a result, we can find the posterior mean $\tilde{\mu}_t$ in the following explicit form:

$$\tilde{\mu}_t(\mathbf{x}_t, \mathbf{x}_0) := \frac{\sqrt{\bar{\alpha}_{t-1}} \beta_t}{1 - \bar{\alpha}_t} \mathbf{x}_0 + \frac{\sqrt{\alpha_t} (1 - \bar{\alpha}_{t-1})}{1 - \bar{\alpha}_t} \mathbf{x}_t \quad (6)$$

$$= \eta_t \mathbf{x}_0 + \xi_t \mathbf{x}_t. \quad (7)$$

By plugging Eq. (6) into Eq. (2), and choosing a parametrization that matches μ_θ to $\tilde{\mu}_t$ at each diffusion step t , for example $\mu_\theta(\mathbf{x}_t, t) = \eta_t g_\theta(\mathbf{x}_t, t) + \xi_t \mathbf{x}_t$ (where g_θ is

a function that directly predicts \mathbf{x}_0 from \mathbf{x}_t), we arrive at an objective function at diffusion step t :

$$\min_{t, \mathbf{x}_0, \epsilon} \mathbb{E} \left[w_t \|\mathbf{x}_0 - g_\theta(\mathbf{x}_t, t)\|^2 \right] \quad \text{for } t = 1, \dots, T-1. \quad (8)$$

where $w_t := \eta_t^2 / 2\sigma_t^2$ and t is absorbed into the expectation instead of being summed over.

A.2. Noise schedule and loss weights

We work with the so-called *linear* noise schedule [19], defined as:

$$\beta_t = (T - t) / (T - 1) \cdot \beta_1 + (t - 1) / (T - 1) \cdot \beta_T, \quad (9)$$

where $t = 1, \dots, T$, $\beta_1 = 10^{-4}$ and $\beta_T = 0.02$. We tried several different ones, and found that this offered the best combination of PSNR and FID/256. We provide an ablation in Appendix C.3.

We reweight the individual loss terms from Eq. (8) to $w_t = 1$, inspired by the choice of Ho *et al.* [19], who do the same for the loss formulation that predicts the noise instead of the denoised sample. The theoretically derived $w_t = \eta_t^2 / (2\sigma_t^2)$ result in extremely large weights for small t , as seen in Fig. A.1. We find that $w_t = 1$ works better, likely because of the more evenly distributed loss scales, but it is possible that better weightings exist. Note that the reweighting of the ϵ -objective of Ho *et al.* results in different weighting than $w_t = 1$ due to the reparametrization.

A.3. Motivation for modeling residuals

DIRAC outputs an initial reconstruction $\tilde{\mathbf{x}}$, then models the distribution of residuals $p(\mathbf{r}|\tilde{\mathbf{x}})$ using a DDPM, where $\mathbf{r} = \mathbf{x} - \tilde{\mathbf{x}}$ (we drop the index 0, which denotes the data space for our diffusion model). In theory, one could model the image distribution $p(\mathbf{x}|\tilde{\mathbf{x}})$ directly. From an entropy perspective, the two approaches are equal: the entropy of $p(\mathbf{r}|\tilde{\mathbf{x}})$ is equal to the entropy of $p(\mathbf{x}|\tilde{\mathbf{x}})$ since, given the data \mathbf{x} , the residual \mathbf{r} is a deterministic function of the initial reconstruction. Yet, while their entropy might be similar, the shape of these distributions is different.

In Fig. A.2, we show the histogram of pixel values in the target images (left) and the residuals (right) for each RGB channel, for randomly varying rate factors λ_{rate} . We observe that residual values approximately follow a normal distribution, whereas the pixel values in image space show a more intricate distribution. Given the fact that DDPMs (in their typical formulation) map Gaussian noise to the target distribution, we conjecture that it is desirable that the target distribution is close to a normal distribution, and that it helps reduce the number of sampling steps required to obtain satisfactory perceptual quality. Moreover, the residuals never exceed the bounds of image values, i.e. $[-1, 1]$, so that the

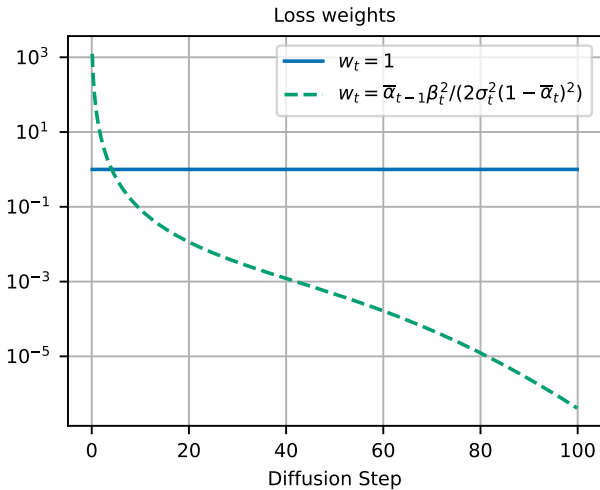


Figure A.1: Comparison of magnitudes for the theoretically derived loss weights and our reweighting ($w_t = 1$).

typical clipping to this range during sampling has no effect. As a result, we introduce rate-dependent thresholding, which we explain in more detail in Appendix A.4.

A.4. Details on sampling procedure

We use this section to provide more details on the sampling in our diffusion. Specifically, we describe 1) the early stopping that results in a smooth transition between high fidelity and high perceptual quality, 2) the late-start sampling, which allows us to skip many more steps than earlier works [38], and 3) the *rate-dependent thresholding* we propose. The observed speedup in sampling corroborates earlier findings [19, 44].

Early stopping The DDPM enhancement model of DIRAC predicts the (often sparse) residual $\mathbf{r}_0 = \mathbf{x} - \tilde{\mathbf{x}}$. We find that we are able to stop sampling at any point before we reach the final step, by simply using the intermediate prediction for the residual $\mathbf{r}'_0(t) = g_\theta(\mathbf{r}_t, t)$ as the final sample. Specifically, we observe that during sampling, early intermediate predictions are close to zero, and that they become sharper over time. Stopping early then typically means higher PSNR, whereas stopping late results in high perceptual quality. Intuitively, this makes sense as well: we know that in the limit of perfect models, $\tilde{\mathbf{x}}$ has the highest possible expected fidelity, and the DDPM can only increase quality by decreasing fidelity.

Stopping early in this manner is somewhat similar to the scheme proposed by Ho *et al.* [19], who use this intermediate prediction to describe a progressive coding scheme. However, we have already transmitted the initial reconstruction $\tilde{\mathbf{x}}$, and all DDPM sampling happens on the receiver

side, so the settings are quite different. It is the receiver-side generation of residuals that allows to navigate the the distortion-perception tradeoff [8], and that enables early stopping to achieve a desired tradeoff or to reduce compute requirements. Optimizing sampling trajectories of diffusion models is an active field, and further research on the sampling in different (conditional) settings may lead to actionable insights [11].

Late start Similar to findings of [44] and [38], we observe that it is possible to skip several sampling steps. In particular, we take an initial noise sample and scale it to match the expected standard deviation at timestep t given by the forward process, then plug this “latent” into the reverse process. In our case this means $\mathbf{r}_t \sim \mathcal{N}(0, \sigma_t^2 \mathbf{1})$. Nichol *et al.* [44] mainly use the late-start observation to motivate the use of a different noise schedule. Based on the similarity of our observations to theirs, it is possible that there are noise schedules that are better suited for the image compression setting, but we tried several different ones and found that our choice worked best out of the ones we tested (see Appendix C.3). The key finding in our work is that we can skip a large part (up to 80%) of the initial steps without performance degradation.

Rate-dependent thresholding Typically, diffusion works clip the latents to the $[-1, 1]$ as it corresponds to the normalized image-space. Yet we observe that both ground-truth and DIRAC-predicted residuals occupy a smaller value range than $[-1, 1]$. We seek to make better use of clipping, and adjust it to the data range at hand. However, early experiments adjusting the clipping thresholds to a single smaller value—based on range percentiles from the training data—did not improve performance. Instead, we set rate-dependent thresholds for clipping, choosing the thresholds such that 95% of residuals in the training data fall within that range, at the given rate factor λ_{rate} .

We perform this analysis for 20 different λ_{rate} , and the resulting thresholds range from 0.0706 at the highest rate to 0.1490 at the lowest rate. At test time, if the desired λ_{rate} is not in the available set, we use the thresholds from its nearest neighbor.

B. Implementation details

B.1. Reproducibility

Datasets All datasets used in this work are publicly available. We show our three-step data augmentation pipeline for DDPM training in Section 4.1 under Datasets.

To compare to Kawar *et al.* (DDRM) [28] and QGAC [15], we use the Imagenet val-1k dataset. The Imagenet val-1k set consists of the first image from each class in the validation set, alphabetically ordered, as reported in [45].

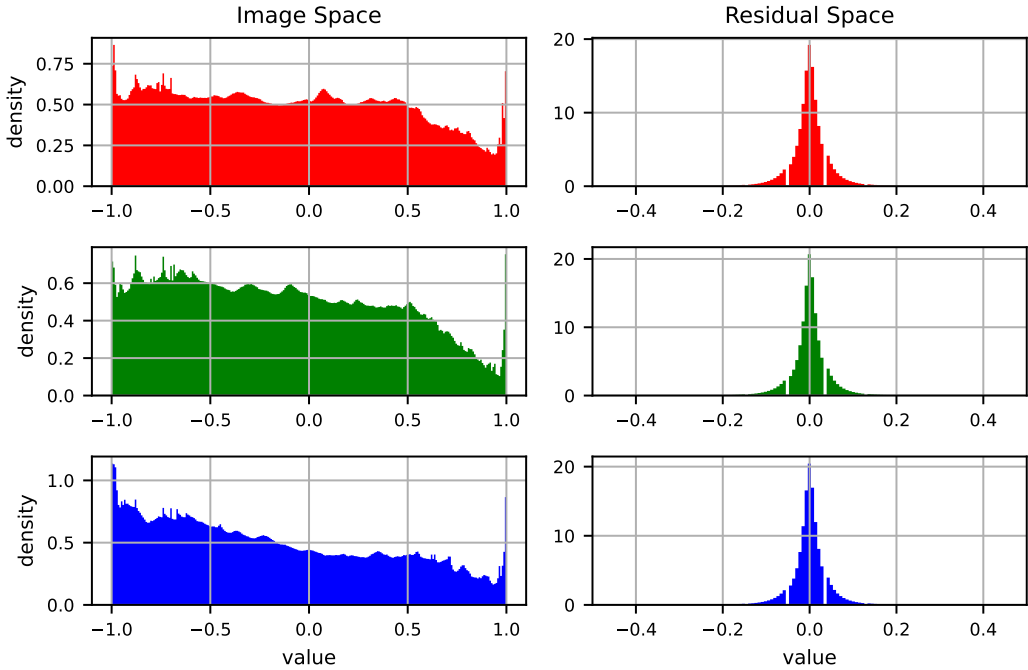


Figure A.2: Distributions of pixel values in a 1000 random 256×256 crops of the CLIC train dataset, left for the target image \mathbf{x} , right for the residual $\mathbf{r} = \mathbf{x} - \tilde{\mathbf{x}}$ where the initial reconstruction $\tilde{\mathbf{x}}$ is from our SwinT-ChARM base model, using random λ_{rate} values. Rows corresponds to the red, green and blue channels respectively.

The exact filenames can also be found in the [corresponding Github repo](#). For direct comparison to Kawar *et al.* [28], we use the data augmentation procedure shown in [their Github repo](#) during evaluation: a square center crop the size of the shortest dimension, followed by a resizing to 256×256 .

To compare to Palette [54] and IIGDM [59] in Appendix C.2, we use the Imagenet ctest10k dataset. The Imagenet ctest10k subset consists of 10,000 images from the Imagenet validation set, as originally reported by [33]. The original page is no longer online, but a copy of the filenames can be found on [Github](#). We use PIL to resize each image so that the shortest side is of size 256, then perform a 256×256 center crop.

Finally, to compare to ArabicaPerceptual [67] in Appendix C.2, we use the CLIC 2022 validation dataset [64], which is comprised of 30 high-resolution images. Note that due to its small size, it makes it unreliable for FID/256, hence we only report LPIPS as proxy for a perceptual metric.

Models The base neural image codec is a variation on a mean-scale hyperprior [5] called the SwinT-ChARM hyperprior [77]. High quality implementations of neural image codecs are available via [CompressAI](#) [6], see for example this [mean-scale hyperprior implementation link on GitHub](#). This library also provides entropy coding functionality. A

reproduced version of the SwinT-ChARM model is [provided on GitHub by user Nikolai10](#). We provide more details on the neural base codec in Appendix B.2.

Reconstructions for standard codecs were obtained using CompressAI [6]. The commands to reproduce these are given in Appendix B.3.

The DDPM component was trained using the open source implementation of [13]. The main change in implementation is that our DDPM is conditioned on an initial reconstruction from a mean-scale hyperprior, which is achieved by concatenating it with the DDPM latent (these two tensors have the same spatial dimensions). We provide information about hyperparameters in Appendix B.4. Lastly, we provide information about computational complexity and training compute in Appendix C.4.

B.2. Neural base codec

Training a neural base codec is a two stage process: we first train a base model for a single bitrate for 2M iterations, then finetune it to operate under multiple bitrates for 500k iterations. Hyperparameters for these two stages are shown in Table B.1.

Single rate SwinT-ChARM We use the “SwinT-ChARM hyperprior” architecture of Zhu *et al.* [77] as neural base codec. This is a hierarchical VAE with quantized latent

Table B.1: Hyperparameters at each stage of training.

Parameter	Single rate	Multi-rate	
	SwinT	SwinT	DDPM
Steps	2M	500k	650k
Learning rate	1e-4	1e-4	1e-4
Batch size	8	8	64
λ_{rate}	0.0016	random	random
λ_{LPIPS}	0.0065	0.0065	0.001

Table B.2: Hyperparameters for our SwinT-ChARM model.

Parameter	Enc/Dec	Hyper Enc/Dec
Patch size	2	2
Embed dim	64	64
Window size	8	4
Blocks	[2,2,6,2]	[4,2]
Head dims	32	32
Normalization	LayerNorm	LayerNorm
Code channels	320	192

variables, similar to the mean-scale hyperprior of Ballé *et al.* [5]. The encoder and decoder networks are built using Swin Transformers [35]. The first level encoder and decoder produce the quantized latent variable and decode it to a reconstruction. The second level, which is the prior model, uses a hyper-encoder to produce a so-called quantized hyper-latent \mathbf{z} , then maps that to parameters $\mu_{\mathbf{y}}, \sigma_{\mathbf{y}}$ using a hyper-decoder. The hyper-latent distribution is modeled using an unconditional prior $p(\mathbf{z})$ [5], so that the hyper-latent can be transmitted losslessly using entropy coding. The probability of the quantized latent under the prior is then equal to $p(\mathbf{y}|\mathbf{z}) = \mathcal{N}(\mathbf{y}|\mu_{\mathbf{y}}, \sigma_{\mathbf{y}})$.

The encoder and decoder contain transformer blocks at four resolutions, the hyper-encoder and hyper-decoder at two resolutions. Special care must be taken to ensure that the latent resolution is a multiple of the hyper codec window size. To enable transmission of images that result in latents with spatial dimensions not divisible by this factor, we use ‘replicate’ padding to pad the image, transmit the padded image, then crop to the original resolution on the receiver side. We transmit the original spatial dimensions as 16 bit integers. This bit cost is negligible compared to the cost of transmitting the content.

We use 320 channels for every layer in the encoder/decoder, and 192 channels for the hyper-encoder/hyper-decoder. Latent quantization is performed using a “mixed” strategy: both decoders see the quantized latents during training, and a straight-through estimator is used to make sure gradients pass through the hard quantization operation; the prior computes the loss based on

latents quantized using additive uniform quantization noise $\mathbf{u} \sim U(-0.5, 0.5)$ [16]. For more details and architecture visualizations, we refer the reader to [77, 35]. Our used hyperparameters are listed in Table B.2.

Multi-rate SwinT-ChARM To obtain a multi-rate base codec, we first train a single rate SwinT-ChARM hyperprior for 2 million iterations using $\lambda_{\text{rate}} = 0.0016$. Multi-rate capabilities are added to this model using a technique known as latent scaling [10, 37]. This procedure effectively changes the latent quantization binwidth by *scaling the latent variable* according to the tradeoff parameter λ_{rate} .

We achieve this in practice by mapping λ_{rate} to a scaling value s using an exponential map:

$$s = \alpha_s \exp(\beta_s \cdot \log \lambda_{\text{rate}}) = \alpha_s (\lambda_{\text{rate}})^{\beta_s}, \quad (10)$$

where α_s and β_s are learnable parameters. Other parametrizations are possible too, this parametrization has the advantage that s is positive if $\alpha_s \geq 0$, thus avoiding instability. The unquantized latent is multiplied by this quantized scalar s before being passed to the prior and quantization. The scaling value s is transmitted as a 16 bit integer at negligible cost. On the receiver side, the latent is divided by s after decompression, before being passed to the decoder.

Enabling the model to operate under different bitrates, and learning α_s and β_s , then requires that we sample different λ_{rate} during training. For each training batch, we sample a value $\lambda' \sim U[0, 1]$. The final sampled tradeoff parameter λ_{rate} is then obtained via interpolation in log space between a pre-specified minimum and maximum:

$$\log_2 \lambda_{\text{rate}} = (\log_2(\lambda_{\text{max}}) - \log_2(\lambda_{\text{min}})) \times \lambda' + \log_2(\lambda_{\text{min}}), \quad (11)$$

where we choose $\lambda_{\text{max}} = 0.0160$ and $\lambda_{\text{min}} = 0.0004$. Given λ_{rate} , the multirate codec—which now includes the original single rate model and the parameters α_s, β_s —is trained using a rate-distortion loss.

At test time, the user picks the rate-distortion operating point by selecting a λ_{rate} value. The mapping in Eq. (10) is used to get the corresponding scalar s for latent scaling. We find in practice that latent scaling, when compared to schemes similar to the one-hot conditioning of [60, 50], performs slightly better near scale $s = 1$, and slightly worse at the extreme bitrates.

B.3. Standard base codecs

VTM base model VTM is the reference implementation of the VVC standard. We run **VTM-17.0**, and use CompressAI [6] to prepare the encoding command. CompressAI converts given input RGB images to YUV444 before coding them in “all intra” mode, then converts the reconstructed YUV444 images back to RGB. These conversions are lossless. We use the default all intra configuration, and use QPs

$\{22, 27, 32, 37, 40\}$, where higher QPs corresponds to low bitrate and vice versa.

Specifically, let $\$V\text{TM}$ be the path to the VTM-17.0 folder, and $\$I\text{MAGEFOLDER}$ be the path to an input image folder. The command used to gather VTM-17.0 evaluations is then:

```
python -m compressai.utils.bench vtm
$IMAGEFOLDER
-c $V\text{TM}/cfg/encoder_intra_vtm.cfg
-b $V\text{TM}/bin
-q [22, 27, 32, 37, 40]
```

JPEG base model JPEG is a well-known standard image codec. To produce JPEG reconstructions and bitstreams, we use the JPEG functionality in Pillow. Similar to VTM, we use CompressAI to prepare the encoding command for multiple quality factors:

```
python3 -m compressai.utils.bench jpeg
$IMAGEFOLDER
-q [5, 10, 15, 20, 25, 30, 35, ..., 95]
```

B.4. DIRAC

Assume a multirate base image codec is available. We train the DDPM to enhance the reconstructions \tilde{x} by conditioning on this image-to-enhance. In order to support multiple bitrates, the DDPM needs to see reconstructions for many different λ_{rate} at training time. In practice, this can be achieved by using the λ_{rate} sampling technique used for multi-rate SwinT-Charm hyperprior training, meaning the DDPM will see reconstructions with random compression rates during training. For the VTM and JPEG base models, we follow a similar procedure to sample λ_{rate} , and discretize it to the integer grid so that it can be used as QP or quality parameter. The DDPM is trained for 650,000 iterations, see the hyperparameter settings specified in Table B.1. It is not conditioned on λ_{rate} , as we found it to have no additional benefit.

Many of our U-Net architecture choices were adopted from the open-source implementation of [13], and we refer the reader to [44, 13] for a detailed explanation of all hyperparameters. Table B.3 provides an overview of the hyperparameter settings for the DIRAC model. Horizontal lines separate U-Net parameters and diffusion process parameters.

The channel multiplier corresponds to the increase in width with respect to the base number of channels in each layer. Following [48], we train our largest models using a U-Net with 6 separate blocks, increasing the multiplier every 2 blocks. Self-attention layers are removed from all layers except the bottleneck of the U-Net. We use the linear noise schedule of [44], as we saw better performance with this schedule in early experiments, see also Appendix C.3 for results with different noise schedules.

C. Results

C.1. Additional metrics

In Fig. C.1 we show additional metrics for DIRAC on the CLIC 2020 test dataset, namely Kernel Inception Distance (KID) [7] and LPIPS [42]. KID is a distribution metric and thus not very reliable on Kodak, and we therefore only show metrics for CLIC 2020 test. As for the notation FID/256, we denote KID/256 the KID computed over all 256x256 half overlapping patches in the evaluation dataset.

It is interesting to see that KID/256 paints a similar story to FID/256. MS-ILLM [43] achieves state-of-the-art in KID/256 and remains unmatched by other methods. However, qualitatively we observe DIRAC-100 sample contains relevant details as seen in Section 5.1, Fig. 5. While comparing LPIPS, we see DIRAC-1 and DIRAC-100 achieve similar LPIPS scores, further confirming its lower correlation with human judgement.

C.2. Comparison to enhancement literature

In Fig. C.2, we report two additional sets of results comparing to enhancement literature on slightly different tasks and/or datasets.

The first two plots in Fig. C.2 compare VTM+DIRAC to the latest standard codec Enhanced Compression Model (ECM) [1] and its GAN-based learned in-loop filter methods (*i.e.* enhancement) *Arabic* and *ArabicPerceptual* [67] on the CLIC 2022 val dataset. The work *ArabicPerceptual* [67] is trained with a perceptual loss (LPIPS and discriminator), and is most relevant to our perceptual enhancement work *i.e.*, to be compared to VTM+DIRAC-100.

The right-most plot in Fig. C.2 compares JPEG+DIRAC to the diffusion-based image-to-image models *Palette* [54] and its follow-up work *ΠIGDM* [59]. *Palette* is explicitly trained for JPEG restoration, while *ΠIGDM* introduce an algorithm to re-purpose a pre-trained diffusion model to solve any inverse problem, including JPEG restoration, similar to [27, 28]. While both outperform JPEG+DIRAC in terms of FID (not FID/256) on ImageNet-ctest10k, it is good to remember the comparison might not be the fairest. Both *Palette* and *ΠIGDM* were trained on ImageNet 256x256 resized crops, and hence cater well to low resolution datasets as well as being closer to the test data distribution. JPEG+DIRAC was trained on the much higher resolution CLIC 2020 train dataset. Furthermore, *Palette* has more than 5x the number of parameters of JPEG+DIRAC, and uses 10x the number of sampling steps.

C.3. Noise schedule ablation

The choice of noise schedule can be important for performance [44], and we tried several different options early in our experiments. The so-called *linear* and *cosine* schedules [44] are two popular choices. Because some of our results

Table B.3: Hyperparameters for DIRAC during training and sampling. We refer the reader to the official open source implementation of Nichol and Dhariwal [44] for more details on these parameters.

Parameter	Command line	DIRAC parameter value
Channel multiplier	channel_mult	1,1,2,2,4,4
Base num. channels	num_channels	128
Learn σ_t	learn_sigma	false
Group normalization	group_norm	true
Attention resolutions	attention_	none
Num. attention heads	num_heads	1
Objective	predict_xstart	true
Num. ResBlocks	num_res_blocks	2
Scale shift conditioning	use_scale_shift_norm	false
Diffusion steps	diffusion_steps	1000
Noise schedule	noise_schedule	linear
Use DDIM sampling	use_ddim	true
Resampling timesteps	timestep_respacing	ddim100

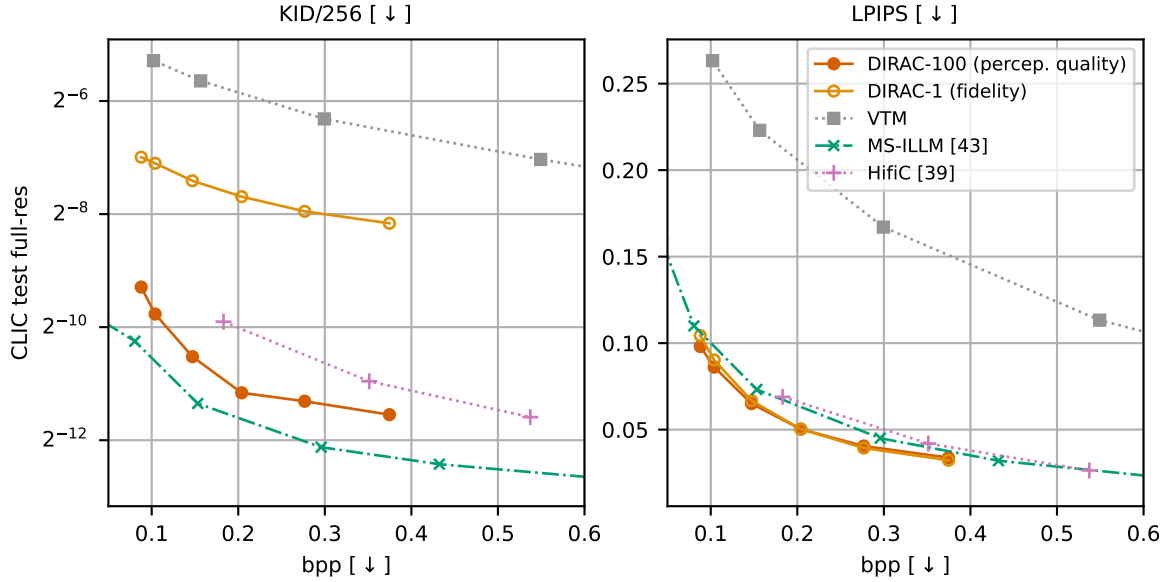


Figure C.1: Additional perceptual and distortion metrics for the CLIC 2020 test set.

suggested that our chosen linear schedule is not ideal (see discussion in Appendix A.4), we also decided to try more extreme approaches, meaning schedules where the decay from sample to 0 (characterized by $\bar{\alpha}_t$) happens either early or very late. For those schedules we devised a generic formula that allows us to model a wide variety of shapes for $\bar{\alpha}_t$:

$$\bar{\alpha}_t(L, p) = \frac{\frac{1}{1+\exp(2L \cdot t^p - L)} - \bar{\alpha}_1(L, p)}{\bar{\alpha}_0(L, p) - \bar{\alpha}_1(L, p)}, \quad (12)$$

where L and p are the parameters that define the shape

of the decay, and a generalized time $t \in [0, 1]$ is used. We define the following three schedules: 1) *early decay* ($L = 5, p = 0.3$), which decays faster than the linear schedule; 2) *late decay* ($L = 1, p = 3$), which decays later than the cosine schedule; and 3) *smooth late decay* ($L = 6, p = 3$), which also decays late, but has close to zero gradient in the final forward steps. All schedules are visualized in Fig. C.3, along with their performance in PSNR and FID/256. We find that the linear schedule offers the best tradeoff between fidelity and perceptual quality. Note that this evaluation was done with intermediate checkpoints

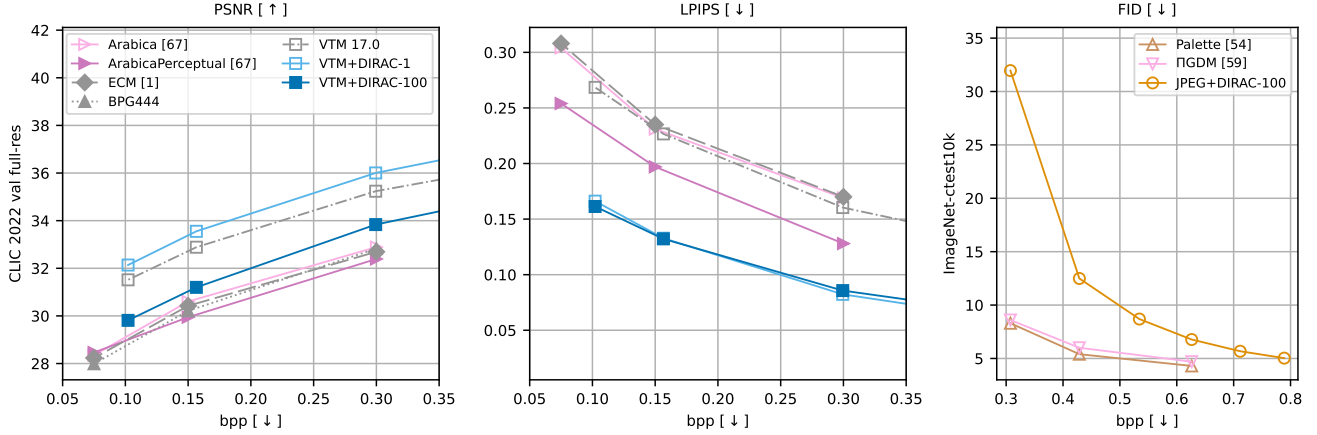


Figure C.2: Additional quantitative comparisons of VTM+DIRAC and JPEG+DIRAC to enhancement literature on CLIC 2022 val and ImageNet-ctest10k respectively. Note that all models were trained on different datasets and have different number of parameters, which does not favor fair comparison. In particular Palette has about 5x the number of parameters as JPEG+DIRAC, was trained on ImageNet low-resolution dataset and is evaluated with 10x the number of sampling steps.

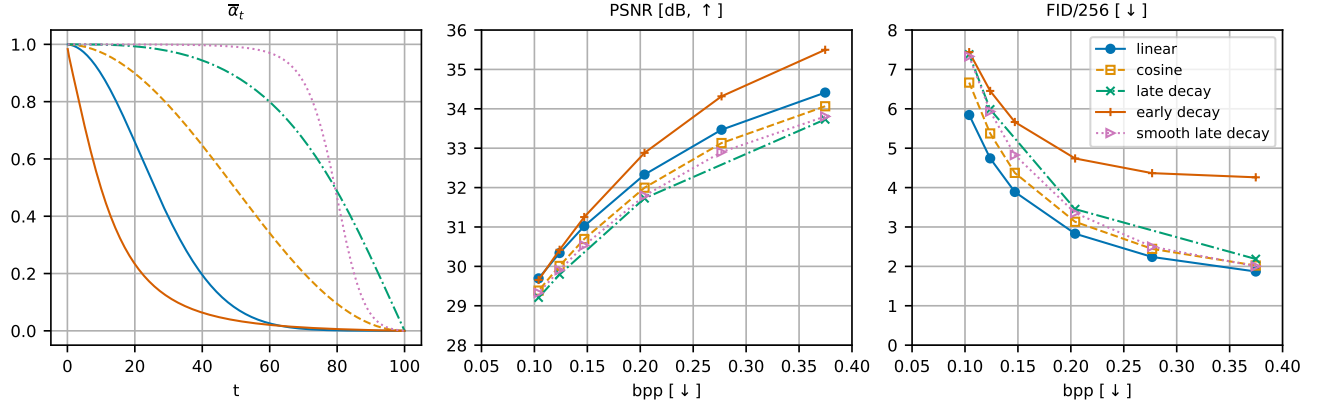


Figure C.3: Shape of the $\bar{\alpha}_t$ curves for the different noise schedules (left panel) and their PSNR and FID/256 performance on CLIC 2020 test (center and right panel). Evaluation done with intermediate DIRAC checkpoints (150k steps).

(after 150k training steps), as we did not continue training with the other schedules.

C.4. Compute

We provide information on the computational complexity of model components, and the cost of sampling, in Table C.1. We run benchmarking on a desktop workstation with a Nvidia 3080 Ti card, CUDA driver version is 455.32.00, CUDA 11.1. We use 1,000 forward passes on square inputs of size 256×256 and 1024×1024 , use GPU warmup, and record inference time using CUDA events. We do not include time to entropy code here.

All our (base codec) multi-rate SwinT-ChARM models were trained on a single Nvidia V100 card. Final DIRAC models were trained on 2 Nvidia A100 cards using data par-

allelism.

A fair comparison between methods would not only require equalization of bitrate, but ideally also equalization of training and test-time compute. For example, HiFiC decoding complexity is substantially lower than that of DIRAC if many sampling steps are used, which will give DIRAC-100 an unfair advantage. DDPMs also see more datapoints than HiFiC during training as a larger batch size is typically used. In this work, we mainly focused on feasibility of the approach, and have therefore not equalized training compute.

Table C.1: Computational complexity. Runtime mean and standard deviation were obtained using 1,000 forward passes, either for a 256×256 or a 1024×1024 input. Note that none of the models here were explicitly optimized for inference speed, numbers are indications only.

	Parameter count	Runtime 256 (ms)	Runtime 1024 (ms)
SwinT-ChARM	28.4M	37.9 ± 0.5	153.8 ± 0.4
DIRAC U-Net	108.4M	37.5 ± 0.8	486.3 ± 1.2
HiFiC	181.5M	17.0 ± 0.4	129.2 ± 0.5

C.5. Texture differences JPEG+DIRAC-1 vs. JPEG+DIRAC-100

In Sec. 5.2, in particular in Fig. 6, we observed little difference in LPIPS on ImageNet-val1k between JPEG+DIRAC-1 and JPEG+DIRAC-100 *i.e.*, between 1 and 100 sampling steps. Upon qualitative assessment in Fig. C.4, it becomes obvious how sampling drastically improves the textures and cleans JPEG artefacts. JPEG+DIRAC-1 gets rid of most of the blocking, and including removal / dampening of wrong color hues, like the typical purple artefact. One of the main failure modes of JPEG+DIRAC is small text and small faces—typical for generative compression models—and both can be seen in example “81815”.

It is good to note that FID/256 on CLIC 2020 test does improve substantially, which better aligns with human judgement. It is yet another signal pointing towards FID/256 as the objective metric correlating best with human evaluation [39]. On the contrary, JPEG+DIRAC-100 always has worse PSNR than JPEG+DIRAC-1, as it measures fidelity but poorly correlates with human judgement.

Finally, for completeness we include the same set of samples for VTM+DIRAC in Fig. C.5. In most if not all cases human judgement would favor VTM+DIRAC-100, although it consistently has worse PSNR. We can see that, contrary to JPEG+DIRAC, small text is better handled. It is most likely due to much better conditioning / starting point. Yet some artefacts can still creep in, as in “d8ed4” where the wine label tends to be “overtextured”.

C.6. Qualitative results

We include more qualitative results below. In Fig. C.6, Fig. C.7, we show crops from images from the CLIC 2020 test set and reconstructions by various image codecs. We include images chosen by [3, 43] to ensure a fair comparison. We match the bitrate to the Multirealism model of Agustsson *et al.* [3]. The HiFiC reconstructions are obtained from a reimplemented HiFiC model, trained for the 0.15 bits per pixel range, and we do not perform bitrate matching.

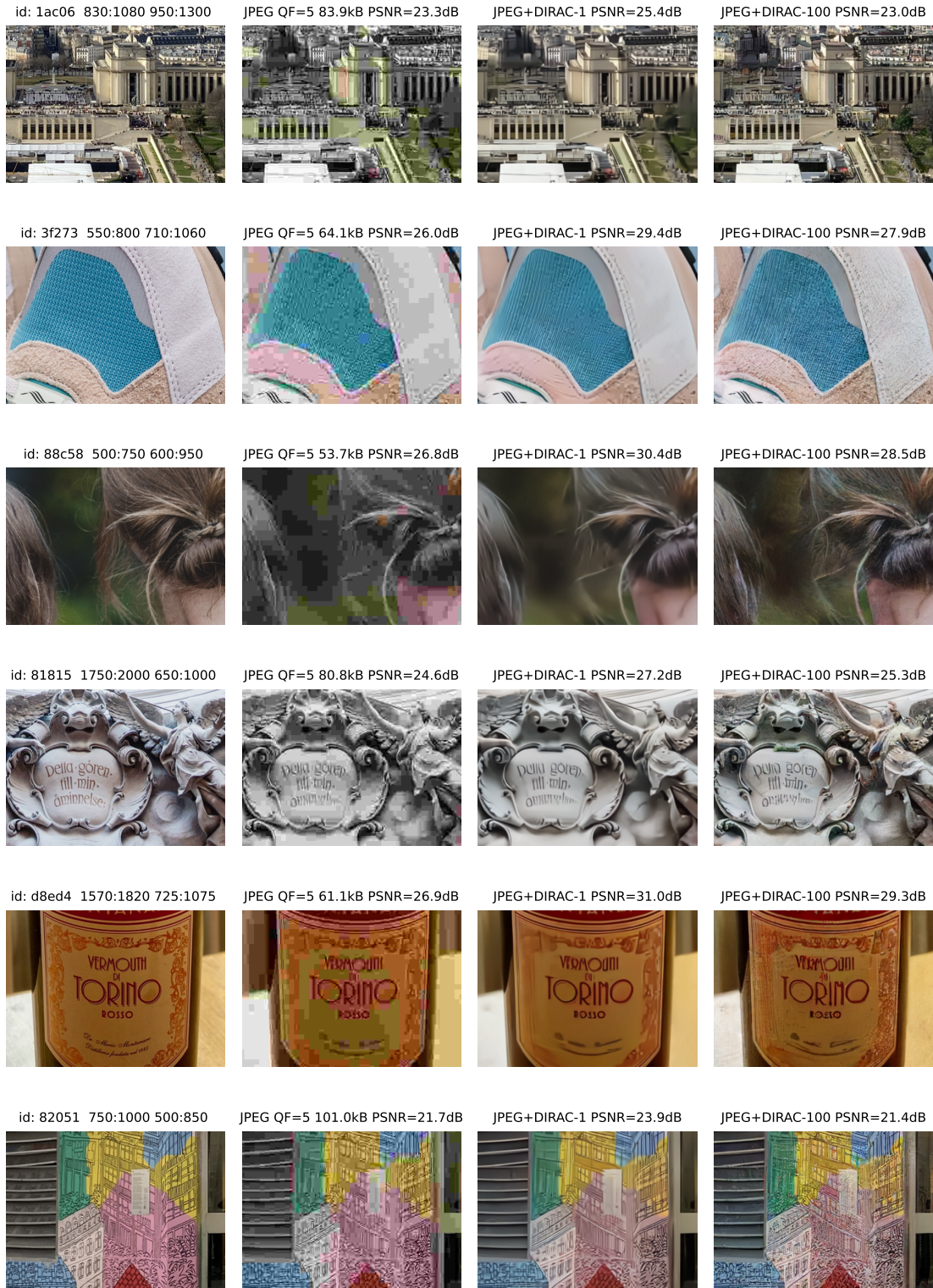


Figure C.4: Samples from the JPEG enhancement model. Note the large texture differences between JPEG+DIRAC-1 and JPEG+DIRAC-100, and the overall drastic improvement over JPEG on CLIC test 2020 crops. Best viewed electronically.

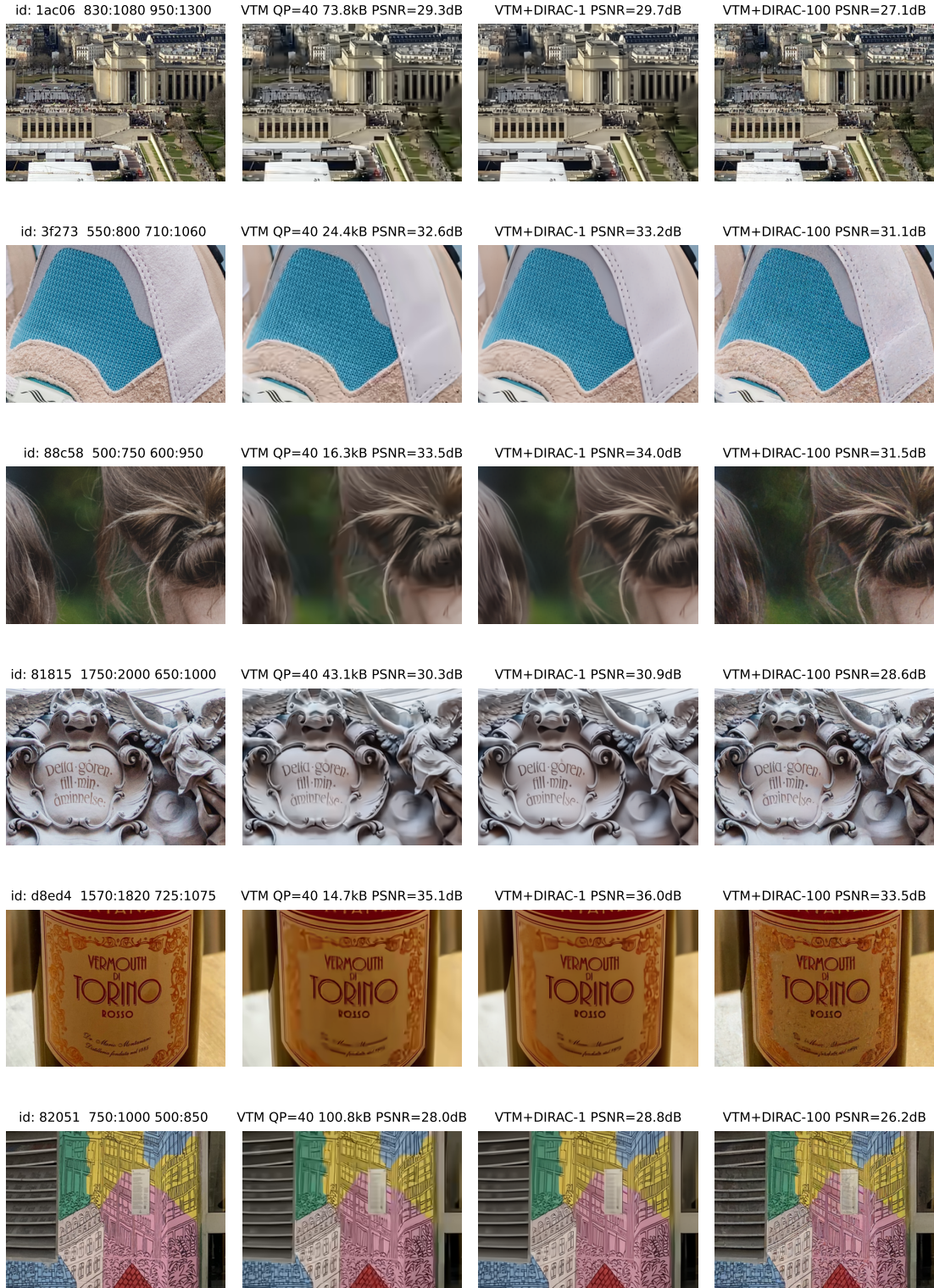


Figure C.5: Samples from the VTM enhancement model. Note the large texture differences between VTM+DIRAC-1 and VTM+DIRAC-100, and the overall improvement over VTM on CLIC test 2020 crops. Best viewed electronically.

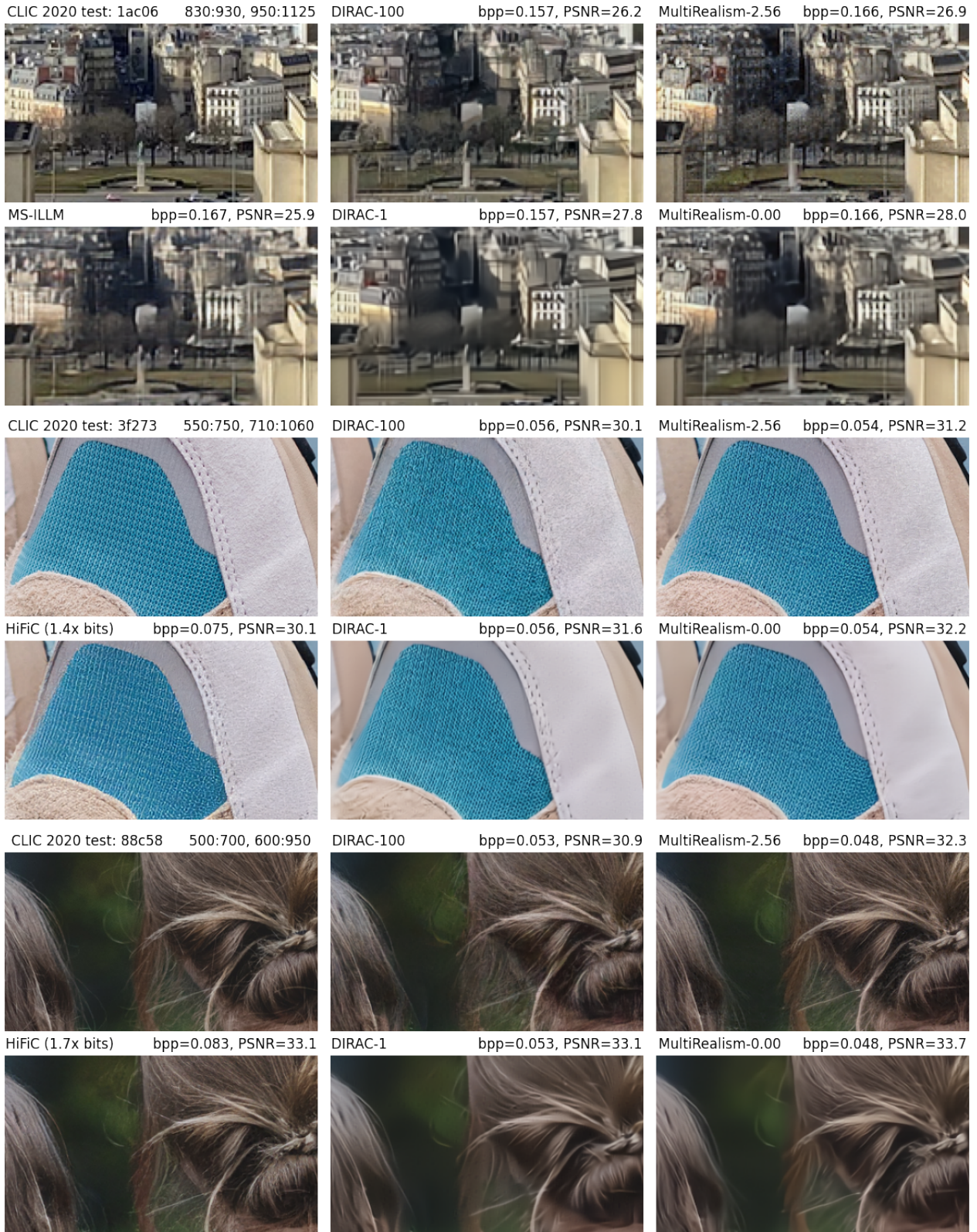


Figure C.6: Reconstructions from various image codecs on CLIC 2020 test data. Crop locations were chosen to match related work to ensure a fair comparison [3, 43]. Bitrates were chosen so that they match the Multirealism baseline [3].

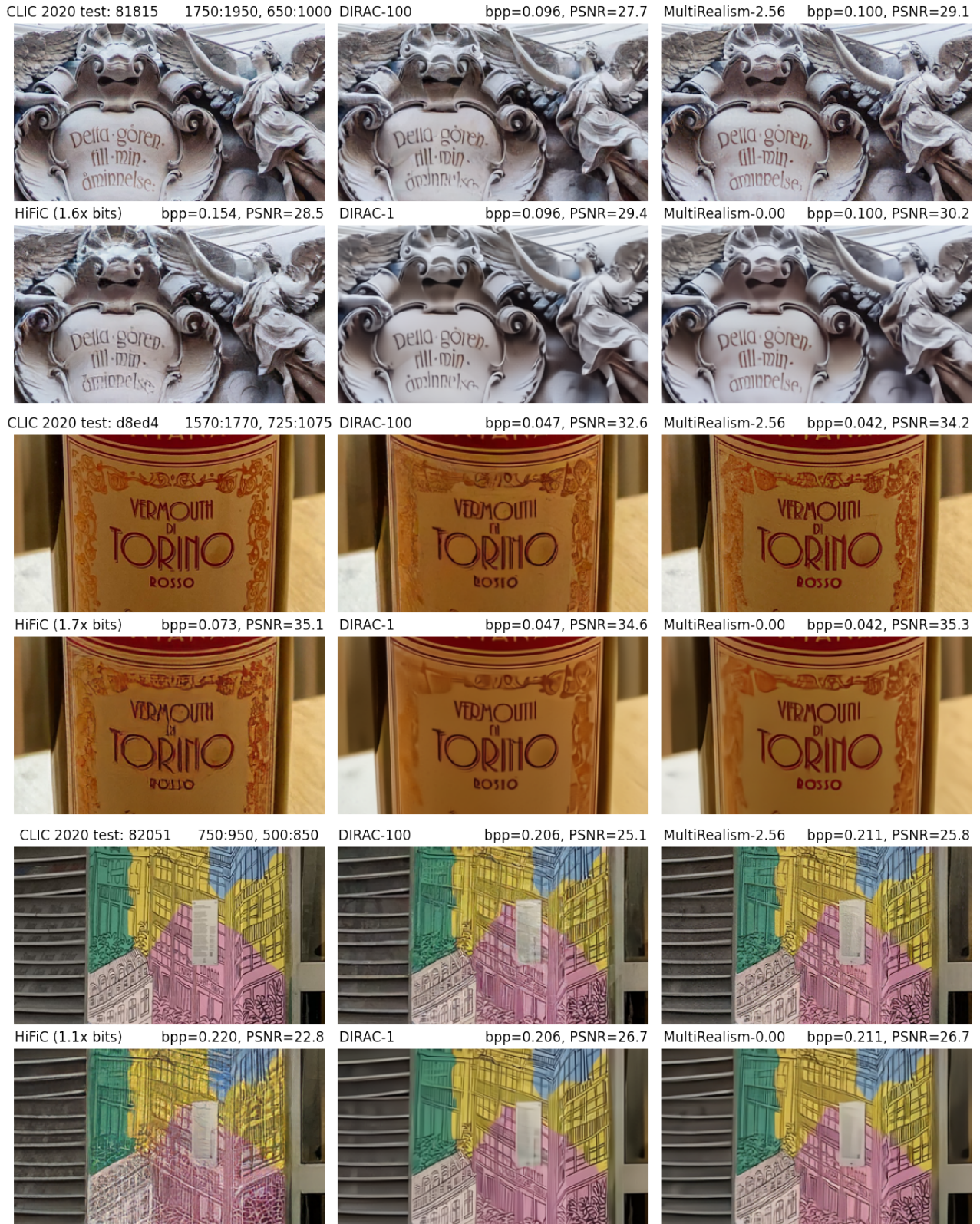


Figure C.7: Reconstructions from various image codecs on CLIC 2020 test data. Crop locations were chosen to show text and salient features such as fine lines and small faces.